Advances in our understanding of pyroclastic current behavior from the 1980 eruption sequence of Mount St. Helens volcano (Washington), USA

Brittany D. Brand, Nicholas Pollock, James W. Vallance, Tomaso Esposti Ongaro, Olivier Roche, Matteo Trolese, Guido Giordano, Aaron A. Marshall, C. William Criswell

Advances in our understanding of pyroclastic current behavior from the 1980 eruption sequence of Mount St. Helens volcano (Washington), USA.

Brittany Brand, Department of Geosciences, Boise State University, 1910 University Drive, Boise, Idaho 83725-1535, USA (corresponding author: brittanybrand@boisestate.edu)

Nicholas Pollock, Department of Geology, Westminster College, 1840 South 1300 East Salt Lake City, UT 84105 USA

James W. Vallance, U.S. Geological Survey, Cascades Volcano Observatory, 1300 SE Cardinal Court, Suite 100, Vancouver, WA, 98683, USA

Tomaso Esposti Ongaro, Istituto Nazionale di Geofisica e Vulcanologia, Sezione di Pisa via C Battisti 53, 56125 Pisa, Italy

Olivier Roche, Laboratoire Magmas et Volcans, Université Clermont Auvergne, CNRS, IRD, OPGC, 63000 Clermont-Ferrand, France

Matteo Trolese, Dipartimento di Scienze, Università degli Studi Roma Tre, L.go S.L. Murialdo 1, I-00146 Rome, Italy

Guido Giordano, Dipartimento di Scienze, Università degli Studi Roma Tre, L.go S.L. Murialdo 1, I-00146 Rome, Italy

Aaron Marshall, Department of Geosciences, Boise State University, Boise, ID, 83725, USA

C William Criswell, Department of Earth and Planetary Sciences, University of New Mexico, Albuquerque, USA

Abstract:

This review summarizes what the volcanology community has learned thus far from studying the deposits of pyroclastic currents (PC) from the 1980 eruption sequence at Mount St. Helens. The review includes mass flow events during the May 18 eruption, including the lateral blast, the afternoon column collapse and boil-over PC activity, and some aspects of the debris avalanche. We also include a summary of PCs generated in the smaller eruptions following the climactic May 18 event. Our objective is to summarize the state of our understanding of PC transport and emplacement mechanisms from the combination of field and laboratory observations, granular flow experiments, and numerical modeling techniques. Specifically, we couple deposit characteristics, experiments, and numerical modeling techniques to critically address the problems of (1) constraining conditions in the flow boundary zone at the time of deposition, (2) the influence of substrate roughness and topography on PC behavior, (3) the prevalence, causes, and consequences of substrate erosion by PCs, and (4) the reconstruction of PC transportation and sedimentation processes from a combination of geophysical and sedimentological observations. We conclude by providing opportunities for future research as our field, experimental, and numerical research techniques advance.

Key Words:

Mount St. Helens; blast; pyroclastic current; pyroclastic density current; flow boundary zone

Statements and Declarations:

The authors have no conflicts of interest related to this publication.

Introduction:

The 1980 eruption sequence of Mount St. Helens (MSH), Washington (USA) is among some of the best-observed and best-studied of our time. The well-exposed and well-preserved deposits distributed across diverse topography provide a natural laboratory to improve our understanding of eruption dynamics and volcanic hazards. This paper highlights and summarizes what we have learned thus far from studying pyroclastic current (PC) deposits from the 1980 MSH eruption sequence. We consider all PC-forming events, including the early lateral blast, boil-over PCs during the afternoon of the May 18, 1980 eruption, and PCs generated in the smaller eruptions following the climactic May 18 event, and also include some aspects of the debris avalanche. We aim to establish an understanding of PC behavior from a combination of field observations, experiments, and numerical modeling techniques, focusing on the following topics:

- Insights into the PC transportation and sedimentation processes from field observations, experiments, and modeling.
- Influence of substrate roughness and topography on PC behavior from field observations and experiments
- Prevalence, causes, and consequences of substrate erosion by PCs

For organization purposes, the paper is split into four sections:

- Directed Volcanic Blasts and Blast-PCs
- May 18, 1980 Plinian Column Collapse and Boil-over PCs
- June, July, and August 1980 PCs
- Temperature measurements of the 1980 MSH PC deposits and their significance

Brief Discussion of PC Terminology and Concepts

Following the justification presented in Palladino (2017), we adopt the more general term of 'pyroclastic current' (PC). This term allows for the further description of the type of the flow without any a-priori assumption about the driving mechanisms. The nature and dynamics governing a PC largely depend on the solids fraction of the current and its stratification profile, the nature of particle-particle and fluid-particle interactions within different regions of a stratified current, shear conditions along the base and fluid shear both within and along the margins of the current, entrainment of the substrate, and entrainment of the ambient air (Dufek, 2016; Lube et al., 2020). PCs conditions include (1) turbulence-dominated, compressible dilute gravity currents driven by their density contrast with the atmosphere, (2) concentrated, ash-rich granular flows where elevated gas pore pressure promotes greater mobility than dry granular flows, and (3) dry granular flows with negligible gas pore pressure where particle-particle interactions control flow behavior. However, gradations between these three flow types certainly exist, and one single current could transition between different flow types over the course of its runout. Note also that flow types (2) and (3) may grade vertically into a dilute current like that of flow type (1).

Below is a brief list of terminology used within this paper:

Co-ignimbrite ash plume. A cloud of fine ash particles elutriated from the main current that overrides a PC. The co-ignimbrite ash plume often buoyantly lofts into the atmosphere after a PC comes to rest. The ash particles then settle as an ash fall deposit, blanketing the PC deposit or falling further downwind.

Flow boundary zone. The zone between the basal transport system and the substrate (Branney and Kokelaar, 2002). The nature of the flow boundary zone is a function of the velocity, shear rate, concentration, deposition rate, rate of supply of sediment from the overlying current, and whether the zone is moving upwards (i.e. depositional) or downwards (i.e. erosional). The flow boundary zone can range from centimeters to meters thick, and both the nature of and processes occurring within the flow boundary zone control the facies of the resulting deposit (Sulpizio et al., 2014).

Granular flow. A type of concentrated (i.e., solids fraction larger than about 0.4) particulate gravity flow in which momentum loss is dominated by particle-particle friction and particle-particle collisions. Friction can be lowered by the presence of an interstitial fluid and its associated pore pressure.

Inertial gravity current. A type of gravity current in which friction is negligible. In particle-driven inertial gravity currents, momentum loss is controlled by sedimentation and air entrainment, which lower the density contrast with respect to the ambient fluid.

Pore fluid pressure. Pressure of the interstitial fluid (gas and suspended fine ash mixture) in a granular mixture, which increases or decreases as the mixture deflates or expands, respectively. Pore-fluid pressure larger than the atmospheric pressure causes fluidization of the granular mixture and increases mobility.

Levée. Lateral margin of a granular flow deposit in which coarse grains segregate and accumulate as the flow propagates downslope. Upstream of lobate termini, these depositional features stand higher than the channel deposits they delimit because the relatively more fluid channel material flowed away (or evacuated) downslope during waning flow after the levées were in place.

Morphodynamic Currents. Currents subject to rapid flow transformation due to interaction with the substrate (erosion, deposition, flow redirection), ambient air entrainment, and related changes to the concentration gradient with distance from source.

Recumbent Flame Structures. A syn-depositional sedimentary structure in which material from a substrate appears to protrude into an overlying deposit but bends and extends in the downstream direction before tapering to a point and pinching out.

Self-channelization. When a granular flow erodes the underlying substrate and creates a channel, resulting in confinement or partial confinement of the flow.

MSH Eruption Summary

MSH is the most active volcano in the Cascade Range. Eruptive activity over the past 40,000 years is dominated by the eruption of dacite domes, tephra fall, block-and-ash flows, pyroclastic flows, and lahars (Mullineaux and Crandell, 1981). MSH is known for its tendency toward explosive behavior.

The 1980-1986 eruptive period began with precursory seismic activity in March 1980 (Christiansen and Peterson, 1981). Within a week of seismic onset, steam explosions created a 400 m diameter crater and two fracture systems that extended across the summit. Phreatic and seismic activity continued through May 17, with more than 10,000 earthquakes recorded over a two-month period. Perhaps most impressive was the dramatic inflation of the north flank, which extended northward subhorizontally at the unprecedented rate of 1.5-2.5 meters per day (Lipman et al., 1981). This rapid inflation, the consequence of magma entering the upper volcanic edifice and ponding as a massive cryptodome, caused a bulge on the north flank that ultimately grew outward 140 m before failing on the morning of May 18, 1980.

At 0832 local time on May 18, 1980, a magnitude 5.1 earthquake was accompanied by a sector collapse of the volcano's north flank and summit, resulting in one of the largest landslide in recorded history (Moore and Rice, 1984). The collapse resulted in three massive slide blocks. The first slide block, with a 600-m-high headwall, crosscut the bulge and exposed the underlying cryptodome (Pallister et al., 2017). Slide block II, which immediately followed the first slide block, removed ~1 km of overburden and rapidly decompressed the underlying magmatic system. Slide block III began two minutes after the initial earthquake (Waitt, 2015; Pallister et al., 2017).

The debris avalanche resulting from the sector collapse traveled northward; part of the debris avalanche surmounted the saddle between Johnston Ridge and Harry's Ridge (up to 900 m of relief), while most of the landslide was deflected westward by Johnston Ridge, flowing ~20 km

down the North Fork Toutle River (Voight et al., 1981; Glicken, 1996). The eastern part of the debris avalanche flowed into Spirit Lake, depositing hummocks along the base of the ridges on the north side of the lake. Water displaced by the debris avalanche resulted in a 265 m high water wave, which extended along the steep banks on the opposite sides of the lake (Waitt, 2015). The ~2.5 km^3 debris avalanche covered 60 km^2, with a runout distance of about 23 km (Voight et al, 1981). The average depth of the deposit is 45 m, although locally it is up to 180 m thick. The debris avalanche left a hummocky terrain of shattered slide blocks across its flow path, including in the shallow-dipping plain just north of the volcano flank.

The sector collapse caused rapid decompression of the underlying magmatic systems, triggering a series of closely spaced directed volcanic explosions, referred to as the lateral blast (Fig. 1; Christiansen and Peterson, 1981; Moore and Rice, 1984). The first explosions began approximately 30 seconds after the earthquake as slide block I detached from slide block II; a second, much larger series of explosions began 60-70 seconds later from behind slide block II (Sousa and Voight, 1995; Hoblitt, 2000). These explosions, composed of fragmented cryptodome material and broken pieces of the volcanic edifice, had a cumulative volume of ~90×10^6 m^3 (~60×10^6 m^3 of dense rock equivalent) (Voight, 1981; Moore and Albee, 1981; Belousov et al., 2007). The expanding mixture accelerated to the north before collapsing to form a stratified, gravity driven PC (Moore and Rice, 1984; Hoblitt, 2000; Esposti Ongaro et al., 2012, Figure 2a).

The blast PC from the first explosion surmounted Johnston Ridge in ~65 seconds; the second blast PC, produced from a much larger explosion, surmounted Johnston Ridge in under a minute and overtook the first PC within ~60 seconds of initiation (Hoblitt, 2000). Both currents rapidly overtook the landslide that was simultaneously propagating northward, as evidenced by eruption sequence photographs and blast deposits found beneath debris avalanche deposits at the base of Johnston Ridge (Glicken, 1996). The blast PC devastated 600 km^2, reaching its furthest runout distance of 30 km in roughly 5 minutes (Fig. 1; Moore and Rice, 1984; Hoblitt, 2000). A co-ignimbrite ash plume rose from the blast, reaching 30 km by 0900 (Criswell, 1987; Figure 2a) and dropping 5-7 mm diameter accretionary lapilli as far as 40 km north of the volcano (Sisson, 1995). The activity resulting in the debris avalanche and blast represents the first of six eruptive phases of the May 18, 1980 eruption (Fig. 3).

The descriptions of Phases II through VI originate from Criswell (1987) unless noted otherwise. The early Plinian phase, Phase II, began after emplacement of the blast with a weak ash plume (Fig. 2b), which increased in height and structure after 0900 (Criswell 2021). Criswell (1987) identified a collapse from the west side of the column between 0849 and 0858, resulting in a PC that traveled to the northwest and down the North Fork Toutle Valley (Fig. 2c). The author interprets this early pyroclastic fountain to represent a vent clearing or enlargement of the conduit (Criswell 2021), enabling a well-developed Plinian column by 0925. However, the deposits from this PC event have yet to be studied in detail. Several small PCs to the upper flanks between 1010 to 1035 (Fig, 2d) accompanied the vertical column (Criswell, 1987). The eruption plume height and mass flux steadily increased throughout the late morning, reaching 17 km at 1200 (Fig. 3).

Phase III, known as the early ash flow phase, began around 1217 with the transition to less convective conditions in the column and the onset of PCs, which 'poured through the crater breach' (Figs. 2e and 3). PC activity created an elongated co-ignimbrite ash plume, which extended 4-7 km to the north of the crater. The Plinian column accompanied the PCs for about 30 minutes but dissipated after 1300. After this time, no vertical flux was witnessed at the vent; instead, it appeared

that the majority of the column collapsed to form voluminous PCs, which is why it is referred to as 'boil-over' activity. Mass flux, interpreted from visual observations of the 'vigor' of the eruption (i.e., a combination of visual factors such as the opacity of the cloud, the development of large eddies in the column, the strong vertical convection), appeared to increase during this time. From 1330 - 1500, PC activity became more episodic; the boil-over activity continued to characterize the initiation of each PC.

PC activity became more vigorous between 1430 - 1500; the 'vigor' was described as a decrease in the time between flows and an increase in the size of the flows. This period marks the transition to Phase IV, the 'climactic' phase of the eruption. The climactic phase, which occurred from 1500 - 1715, is associated with the highest mass flux of the eruption (Figs. 2f and 3; Carey et al., 1990). From 1525 to 1600, PCs engulfed the entire volcano. PCs along the east, west, and south flanks only traveled a few hundred meters; whereas PCs funneled through the breach traveled across the shallow-dipping plain to the north (named the Pumice Plain due to the infill of 1980 PC deposits) and into the North Fork Toutle Valley, up to 8 km from the vent. Eruption intensity then decreased from 1605 to 1620 (Fig. 3). By 1625 a vertical Plinian column resumed, reaching 19 km in height. PC activity largely stopped by 1635. Carey et al. (1990) estimated that the PCs and co-ignimbrite ash of phase IV represents 77% of the mass erupted during the Plinian phases of May 18.

Phase V, known as the late ash-flow phase, occurred between 1715 and 1815 (Figs. 2g and 3) and marks a period of waning eruption energy. The eruption column height decreased to just a few kilometers. A brief increase in eruption energy between 1745 and 1810 produced several PCs to the north that reached the North Fork Toutle Valley and Spirit Lake (Fig. 2h). The final phase, Phase VI, is characterized by a period of weak ash emissions that lasted from 1815 on May 18, 1980 to 25 May 1980 (Fig. 3).

After its cataclysmic May 18 eruption, MSH erupted explosively five more times in 1980 with each eruption producing one to two PCs that reached the Pumice Plain (Table 1). Each eruption consisted of individual Vulcanian explosive pulses whose durations were on the order of tens of minutes. Boil-over or low fountaining of pyroclastic ash, lapilli, and blocks initiated each current. PC initiation to deposit emplacement typically lasted no more than about ten minutes. These eruptions emplaced PC deposits on May 25, June 12, July 22, August 7, and October 16–18. Deposits ran out 4–7 km, spread across areas of 1.7–8.3 km^2, and had volumes of approximately 0.001–0.01 km^3 (Table 1) (Rowley et al, 1981).

Directed Volcanic Blasts and Blast PCs:

The initiation of the May 18, 1980 eruption, with a major sector collapse and directed blast, was transformational to our understanding of volcanic eruption behavior. Prior to the 1980 MSH eruption, hummocky topography was found downslope from many volcanoes, but the interpretation of these large mounds of randomly oriented and often shattered volcanic stratigraphy scattered across the landscape largely eluded scientists. For example, given the brecciated nature of the deposits, early researchers who studied the 1956 Bezymianny eruptive sequence in Kamchatka (Russia) misinterpreted the deposits as the exploded ejecta from the eruption (Gorshkov 1959; 1963). Similar ancient deposits found up to 43 km northwest of Mt Shasta volcano in California (USA) were misinterpreted as small, individual volcanic centers by Diller et al. (1915), and later as glacial moraines and the eroded remnants of Tertiary-aged volcanic rocks

(Williams, 1932; Mack, 1960). Only after the May 18, 1980 eruption of MSH were the Mount Shasta deposits accurately identified as the results of an ~45 km^3 volume debris avalanche deposit that occurred 300,000-360,000 years ago (Crandell et al., 1984; Crandell, 1989). However, deposits of an associated directed blast were not found (Crandell, 1989).

Prior to the 1980 eruption of MSH, the relationship between sector or lava dome collapses, debris avalanche deposits, and lateral blasts were also poorly constrained. Directed blasts are defined as volcanic explosions associated with or triggered by volcanic edifice collapse, often with a significant lateral trajectory (Belousov et al, 2007; Belousov et al., 2020). Directed blasts occur when a partly degassed and crystallized magma body in the upper volcanic edifice rapidly and catastrophically decompresses when unroofed by a major edifice collapse (e.g., Bezymianny and MSH; Belousov et al., 2007) or failure of a lava dome (Soufrière Hills Volcano, Sparks et al., 2002; Voight et al., 2002; Mount Lamington; Belousov et al., 2020). The slope-failure controls direction of the blast, commonly as a laterally-directed explosion or series of explosions that expand in a direction normal to the slip surface. However, recent work at Mount Lamington in Papua New Guinea demonstrates that directed blasts can also have a significant vertical component (Belousov et al., 2020).

At MSH specifically, large-scale collapse of the volcanic edifice triggered rapid decompression of the shallow and partially degassed cryptodome, resulting in the directed blast (Voight 1981; Voight et al. 1981, 1983; Glicken 1998). By comparing similar activity at MSH, Bezymianny, Soufrière Hills volcano, and Mount Lamington, Belousov et al. (2007; 2020) identified three components to a directed blast. An initial *burst phase* results from the rapid decompression of the magma (driven by pressure gradient), causing the mixture of gas and particles (fragmented magma and pieces of the edifice) to expand into the atmosphere. The *collapse phase* occurs when the expanding mixture fails to entrain enough ambient air to become buoyant and collapses toward the ground, thus evolving from pressure-driven to a gravity-driven *blast-PC phase* capable of surmounting significant topography. The blast-PC is a stratified pyroclastic current propagating in a dominantly inertial regime where friction is negligible and momentum loss is controlled by sedimentation and air entrainment, which lowers the density contrast with respect to the ambient fluid.

Blast-PCs vary greatly in scale. For example, the Bezymianny blast devastated an area of 500 km^2, the 1951 Mount Lamington blast destroyed 230 km^2, and the 26 December 1997 blast of Soufriere Hills Volcano on Montserrat only blanketed 10 km^2. The 2010 eruption of Mt. Merapi (Jakarta, Indonesia) also produced high-energy PCs that spread over 22 km^2 and showed striking similarities with the aforementioned volcanic blasts (Komorowski et al., 2013). The MSH blast-PC devastated an area of 600 km^2, spread northward across a 150-degree arc and extended as far as 30 km from source, surmounting several ridges with vertical relief of up to 900 m.

Blast PC stratigraphy – Common characteristics and interpretations

The MSH blast deposits have been studied extensively since 1980 (Hoblitt et al. 1981; Moore and Sisson 1981; Waitt 1981; Walker and McBroome 1983; Fisher et al. 1987; Brantley and Waitt 1988; Kieffer and Sturtevant, 1988; Fisher 1990; Druitt 1992; Sisson 1995; Bursik et al. 1998; Belousov et al., 2007), providing not only a way to identify characteristic depositional features, but also insights into the nature of the current that formed them. Fisher (1990) identified a proximal, medial, and distal zone, defined by the degree to which the organic forest litter (duff) is eroded and by the thickness of the blast-PC deposits (Fig. 1). Trees within these three zones were

toppled, except for a few isolated tree stands on the lee side of obstacles (Waitt, 1981; Gardner et al., 2018). The proximal zone, which extends up to 11 km from source, is the area where erosion of the paleo-substrate is the greatest; organic forest litter in unprotected areas facing the volcano was completely removed in this zone. The blast-PC deposit is thicker and coarser in this region. The medial zone extends 1-4 km beyond the proximal zone to the northwest and up to 11 km from the proximal zone to the northeast. The duff layer in areas facing the volcano is discontinuously eroded, and the blast-PC stratigraphy is thinner and finer-grained and, in some locations, completely absent. The distal zone extends from the medial zone 7-15 km to the northwest (down the North Fork Toutle River), from <1 to 6 km to the north, and <2 km to the east. Underlying soil and duff within the distal zone are largely uneroded, and the blast-PC stratigraphy is on the order of cm-thick. A final zone, called the singed 'standing dead' zone, designates where trees were left standing but singed, extends <1 - 5 km to the northeast, 1 km to the north, and <1 km to the east (Fig. 1). Blast-PC deposits are largely absent in this zone except for a scattering of coarse ash across the ground (Druitt, 1992).

It is clear from field investigations that topography influences deposit distribution and runout distance. The blast-PC traveled farthest to the northwest where valleys and ridges were dominantly parallel to the blast flow direction. On the contrary, the blast-PC had the shortest runout to the east, where most of the ridges were perpendicular to the current direction (Fig. 1). In addition, evidence of flow separation around topographic obstacles includes tree blow-down patterns, such as downed trees aligned perpendicular to each other downstream of obstacles, and repeated stratigraphic layers (Fisher, 1990). However, the more recent work of Esposti Ongaro et al. (2011, 2012), described in the next section, demonstrates that blast-PCs dynamics are essentially inertial; that is, while they can be topographically influenced, they are not controlled by the interaction with the topography.

Gardner et al. (2018) uses the distribution of tree stands in the blowdown zone, mostly found where the blast-PC reached ~95% of its runout distance, to estimate the relative density of the blast-PC at those locations. Their modeling results indicate that liftoff on the downstream side of obstacles decreased bulk density because of entrainment and heating of air as the current traveled over a substantial upstream ridge, causing the current to temporarily 'lift off' before collapsing back to the ground and continuing course. They argue that a lack of liftoff in more proximal zones was the result of the current having higher density (because of higher concentration of particles). This phenomenon and the general deposit distribution show how topography and sedimentation from the turbulent flow influences blast-PC dynamics, and how evidence such as tree blow down patterns can be used to constrain the depositional properties of the current.

Comparison of MSH blast-PC deposits to those generated during the laterally-directed blasts at Soufrière Hills and Bezymianny reveal a common stratigraphy that typically exhibits four layers, labeled A, B, C and D (from bottom to top; Belousov et al., 2007; Figure 4); these layers correspond to layers A0, A1, A2, and A3 of Fisher (1987; 1990) and Druitt (1992). They vary in thickness laterally and with respect to topography. We adopt the stratigraphic labeling of Belousov et al. (2007) for ease of comparison to other blast-producing volcanic centers.

Layer A overlies an erosive contact with the paleo-surface (Fig. 4). It is very poorly sorted and contains abundant substrate material (vegetation, dispersed soil, wood fragments, pre-1980 pumice, and sheared soil clots); substrate material composes >90% of the deposit in some

locations. Woody debris in this layer is largely uncharred. Layer A is thickest in the proximal zone, where it contains up to 5 distinct layers, but becomes more massive and thins with distance from source. The erosive contact and incorporation of the substrate indicates rapid deposition after a period of intense erosion, interpreted as the result of turbulent boundary shear between the head of the current and the substrate (Fisher et al. 1987; Fisher, 1990; Belousouv et al., 2007). Lenses of Layer B are sometimes found toward the top of Layer A, suggesting that shearing of layer A by the overriding body of the current continued after its deposition.

Layer B is massive, clast-supported, and fines-depleted (Fig. 4). This layer ranges from ungraded, reverse graded along the base (Fisher 1990; Druitt 1990), and faintly normal graded (Hoblitt et al. 1981). Vegetation and wood fragments, when present, are charred; however, Layer B contains little substrate material relative to Layer A. Layer B is thickest in proximal zones, in topographic lows, and in the lee of obstacles, but thins and fines across topographic highs and with distance from source (Fisher et al, 1987; Fisher, 1990; Druitt, 1990). The massive nature of Layer B suggests rapid suspension sedimentation from a relatively thin (with respect to the current thickness), concentrated, flow boundary layer at the base of the stratified current. The lack of fines suggests elutriation during suspension sedimentation (Fisher, 1990; Druitt, 1990; Belousov et al., 2007), but it is also compatible with sedimentation by large-scale eddies in the turbulent regime by unrolling and margin mechanisms (Lube et al., 2020). Deposit distribution, including thickening in topographic lows and thinning over ridges, suggests that deposition of the layer develops behind the current head.

The contact between Layer B and C is sharp in proximal locations but becomes gradational in the medial to distal zones. Layer C is a fines-enriched, matrix-supported, poorly sorted, massive deposit (Ca, corresponds to A2a of Fisher, 1990) that grades vertically into a laminated cap (Cb, corresponds to A2b of Fisher, 1990; Figure 4). Gas escape pipes commonly overlie buried vegetation. Like the previous layers, Layer C thickens in topographic lows and behind obstacles, and thins along topographic highs. However, thickness changes relative to Layer B are less pronounced, and the deposit, in general, thins more slowly with distance from source, thinning dramatically only in the distal reaches of the deposit (Druitt, 1992). The massive portion of this deposit is interpreted to represent rapid sedimentation under moderately concentrated conditions; whereas, laminated parts of the deposit suggest some degree of traction transport during deposition and thus implies a more dilute, waning phase of the current (Druitt, 1992; Belosouv et al., 2007).

Layer D is a thin (relative to layers A-C), fines-rich, accretionary lapilli-bearing massive deposit (Fig. 4). It is interpreted as ash fallout from the dilute upper portion of the current or a co-ignimbrite ash plume.

In summary, the depositional sequence can be explained by the passage of an initial erosive flow head, which incorporates substrate material into the current but is immediately followed by rapid sedimentation of coarser particles in suspension (Layer A). Layers B and C form behind the head during passage of the body of the current (Druitt, 1992; Belousov et al., 2007). They are a result of rapid sedimentation from a concentrated zone at the base of the stratified flow (Layer B). The stratified current becomes progressively less concentrated as the deposit progressively aggrades and the current evolves, with the less concentrated conditions leading to rapid sedimentation of finer-grained material followed by some degree of traction transport as the basal region becomes more dilute (Layer C; Druitt, 1992; Belousov et al., 2007). The sequence is capped by co-

ignimbrite ash fallout (Layer D). Given the thin and easily erodible nature of these layers, it is not surprising that they remain difficult to identify and accurately interpret for past eruptions.

Combining field characteristics with multiphase modeling to better understand the structure of blast-PCs, dynamic pressure conditions, and nature of the flow boundary zone

Visual observations and geophysical data collected during the blast-phase of the eruption constrain the initial blast front velocity, which moved at 100 - 110 m s^{-1} with local speeds up to 130 m s^{-1} (Voight, 1981; Moore and Rice, 1984), and duration of the flow (~5 minutes; Moore and Rice, 1984). In addition to the insights gained from visual observations and deposit characteristics (e.g., Fisher, 1990; Druitt, 1992; Belousov et al., 2007), there are excellent constraints on the vent geometry and high resolution digital elevation models of the surrounding topography. This combination of data makes MSH an excellent case study to test and validate numerical simulations of the blast mechanism and subsequent PCs, allowing researchers to address how source conditions, such as magma discharge volume, gas content and overpressure, together with vent geometry and topography, control the dynamics and damage potential of blast-PCs.

The dynamics of the MSH lateral blast are controversial in the literature because of the complex interplay between the effects of mixture compressibility and gravity. Sedimentological works, including Hoblitt et al. (1981), Waitt (1981), Druitt (1992) and Bursik et al. (1998), suggest that the deposit features are consistent with the emplacement of a stratified PC that was expanded and turbulent across most of its runout (i.e., beyond about 6 km from the vent). In contrast, Keiffer (1981) modeled the blast as a laterally-oriented under-expanded supersonic jet driven by pressure gradient, in which gravity would be almost negligible because of the very low particle concentration in the mixture. In this view, the observed damage pattern of the blast can be explained by the transition to a subsonic flow occurring through a strong normal shock (Mach disk), whose distance has been estimated between about 5 and 11 km from the source, depending on the initial source conditions (Orescanin et al., 2010). Beyond the Mach disk, the subsonic flow would evolve as a gravity current. The under-expanded jet model demonstrated, for the first time, the key role of mixture compressibility in blast dynamics. However, some of the hypotheses of that work, in particular neglecting gravity and assuming gas-particle equilibrium in a very dilute current, bring into question the relevance of the Mach disk as the actual driver for the transition from the proximal ('direct blast zone') to the medial blast region.

To test the relative importance of compressibility and gravity, Esposti Ongaro et al. (2011, 2012) used the three-dimensional, multiphase flow model PDAC (Pyroclastic Dispersal Analysis Code; Neri et al., 2003; Esposti Ongaro et al., 2007, 2008). PDAC belongs to a family of numerical solvers (including MFIX Dartevelle, 2004; Dufek, 2016; Valentine and Sweeney, 2018; Breard et al., 2020; and ASHEE - Cerminara et al., 2015) able to simulate the fluid dynamics of gas-particle mixtures including the effects of decoupling of particles due to gravity and inertia, energy exchange, turbulent effects including air entrainment, compressibility and the interaction with a rugged topography. The numerical model simulates the evolution of the blast from a set of initial and boundary conditions, representing the state of the exploding mixture at the beginning of the eruption. In particular, the initial conditions used by Esposti Ongaro et al. (2012) were the volume (constrained by the volume of the deposits), pyroclast porosity (derived from petrological studies), gas overpressure (10 MPa constrained by the yield strength of the rocks plus the lithostatic

pressure), and the geometry of the exploding dome (which was defined to drive its expansion to the north). The initial conditions are therefore analogous to those hypothesized by Eichelberger and Hayes (1982) and Alidibirov (1995). The modeled exploding mixture was assumed to fragment instantaneously, and the grain-size distribution was discretized in three bins, according to the available sedimentological data. In particular, three particle classes of equivalent hydraulic diameter of 3,250 μm (35 wt.%; 1,900 kg m^{-3}), 150 μm (37 wt.%; 2300 kg m^{-3}) and 13 μm (28 wt.%; 2500 kg m^{-3}) were used for the juvenile and one particle class of 500 μm (2500 kg m^{-3}) for fragmented country rock and entrained substrate. The simulations included a digital elevation model of the region to explore the interaction with the blast-PC with topography.

Although the PDAC numerical model has the capability to reproduce the features of underexpanded jets (e.g., in Plinian columns; Carcano et al., 2014), the expansion of the eruptive mixture driven by the overpressure with the prescribed blast initial conditions did not evolve into the overexpanded jet predicted by Kieffer (1981) and Orescanin et al. (2010). Multiphase flow numerical simulations indicate instead that, due to the relatively high particle concentration, gravity was effective immediately after the initial expansion phase, inducing the collapse of the eruptive cloud, the obliteration of the shock waves, and the formation of a blast-derived, inertial-dominated PC. The subsequent evolution of the blast-PC is consistent with the observed front advancement velocity, interaction with topography, depositional patterns, inundated area and final runout, and associated buoyant lift-off (Fig. 5).

Numerical simulations reproduced some remarkable consistencies with the depositional patterns of the blast and further support the idea of a turbulent, high energy head followed by a sedimenting body. Esposti Ongaro et al. (2012) find that high shear and high velocities in the flow head promote substrate erosion and efficient suspension of fines, and further argue that their results support the interpretation that the fines-depleted Layer A forms due to rapid sedimentation of coarser particles in suspension immediately behind the flow head. Modelling results indicate that this depositional phase would last around 50 s, at a location 8 km from the eruption source.

Both deposit characteristics and numerical simulations support development of a stratified current behind the flow head consisting of a concentrated, sedimenting basal region grading vertically into a dilute, turbulent current dominated by fines suspension. Esposti Ongaro et al. (2012) argue that rapid sedimentation from the concentrated basal zone of the stratified flow explains Layer B. They find that sedimentation from the current and progressive aggradation of the resulting deposit is most pronounced along the lee side of topographic ridges and associated with enhanced elutriation of fine particles and the rise of convective instabilities, which ultimately contribute to an extensive co-ignimbrite plume. Their model also predicts that the basal flow is more dilute and enriched in fines on ridge crests. These results are consistent with the fines depleted and massive nature of deposits within topographic lows, and the more fines rich nature of the deposits on ridge crests (Fisher, 1990; Druitt, 1992).

MSH blast-PC Summary and Next Steps

This combination of visual observations, damage patterns, deposit characteristics, and multiphase numerical modeling of the MSH blast has improved our understanding of the dominant controls on large-scale PC behavior and dynamic pressure conditions (damage potential). Specifically, rapid decompression of a partially crystalized cryptodome provides the mechanism for magma

fragmentation and initial lateral acceleration of the gas-particle mixture. Collapse of the expanding, dense, fragmented mixture produces blast-PCs with a leading, high shear, high velocity turbulent front that facilitates substrate erosion, followed by a stratified sedimenting body. The highest dynamic pressures, and thus damage potential, are associated with the turbulent head of the current. Topography exerts a strong control on current unloading and fines elutriation within the body of the current, impacting both runout distance (due to sedimentation) and the development of a co-ignimbrite ash plume. The dynamics of the blast-PC after initiation are thus influenced (but not controlled) by topography and the process of particle segregation and current stratification, the latter of which are largely controlled by turbulent diffusion and the nature of the polydisperse multiphase mixture (Eposti Ongaro et al. 2012). The correspondence of numerical model results to some field observations at the macro-scale (e.g., front velocity, runout distance over the rugged topography, impact area, local deposit distribution), obtained with initial and boundary conditions independently constrained by geological considerations (i.e., not obtained by an "inverse" method), provide a model *confirmation*, a fundamental step to the complete model validation (cf. Esposti Ongaro et al., 2020), which supports the reliability of the model for its use in assessing blast-PC impact areas and damage potential for volcanoes worldwide.

Despite the success of the multiphase flow model in reproducing the main large-scale features of the MSH blast-PC, many questions are left open, in particular concerning some of the local features of the blast. The observed damage and the deposit occur in the flow boundary layer, where the turbulent fluctuations of velocity might be very intense, potentially of the same order of magnitude of the main flow, and density can vary significantly due to the competing effects of sedimentation and turbulence. For these reasons, estimates of the dynamic pressure at the base of the current are still affected by severe uncertainty, even by a factor of 10 (Esposti Ongaro et al., 2008). Further progress in modeling capability should be focused on improving the model description and numerical resolution at the base of the currents, including the development of large-scale coherent vortex structures and waves (Brosch et al., 2021), and the dynamics of erosion and of the more concentrated basal layer leading to the deposit. In addition, the source description could be refined, particularly for what concerns the fragmentation process and the emerging grain-size distribution, so far described in numerical models with only three grain size categories. Considering that fragmentation might imply energy consumption corresponding to up to about 4 MPa (cf. Alatorre-Ibargüengoitia et al., 2010), the subsequent blast dynamics would be significantly affected by including such modeling in the initial conditions for blast numerical simulations.

May 18, 1980 Plinian Column Collapse and Boil-over PCs

The afternoon of the May 18, 1980 eruption was dominated by 'boil-over'-style PCs (Fig. 2e, f, and h; Criswell, 1987). In contrast to the blast-PC, the afternoon currents were concentrated, partially fluidized mixtures of ash, pumice, and lithic clasts (Brand et al., 2014). The bulk of the afternoon PCs were funneled through the breach and down the stairsteps, a series of large, 30 to 60 m vertical drops along the northern flank of the volcano, and deposited across the shallow-dipping Pumice Plain (Fig. 1 and 6). However, portions of the PCs also traveled along the steep northeast and northwest flanks during the climactic Phase IV of the eruption, as evidenced by visual observations (Criswell, 1987) and PC deposits (Fig. 6; Brand et al., 2016). Maximum runout distance of the May 18 afternoon PCs was ~8 km to the north (Brand et al., 2014).

Whereas the deposits of the Pumice Plain are dominated by topography-filling massive lapilli-ash, the deposits along the northeast flank include cross-stratified, compound bedforms with form lengths up to 40 m. As we discuss in this section, the differences in facies characteristics are largely controlled by the slope across which the PCs deposited, highlighting the morphodynamic and unsteady nature of such concentrated currents. Indeed, one of the reasons MSH is such an incredible place to study PC behavior is due to the wide variety of topography and surface roughness across which the PCs traveled. In this section, we combine observations of the eruption chronology, deposit characteristics, and deposit distribution with analytical methods to address the following questions:

- How can visual observations of PC activity and deposit characteristics be combined to inform our understanding of PC depositional processes and flow evolution?
- What is the influence of topography on PC behavior and erosive capacity?
- What insights can we gain about PC transportation, erosion, and sedimentation processes from the combination of field observation and experiments?

Primary flow units from the afternoon 'boil-over' PC activity

This section addresses the question: *How can visual observations of PC activity and deposit characteristics be combined to inform our understanding of PC depositional processes and flow evolution*? It summarizes the work of Brand et al. (2014), who present the most extensive work on the well-exposed deposits, but also brings in the work of other authors where appropriate.

Brand et al. (2014) identify five flow units across the shallowly dipping Pumice Plain that correlate to the afternoon PC activity (Figs. 7 and 8). Here we describe and interpret each flow unit with respect to the conditions in the flow boundary zone at the time of deposition. We also correlate each unit with the observations of PC activity and estimates of mass flux from 1215 - 1600 (Fig. 3). Finally, based on our mapping of the area covered and thickness of each flow unit (Tables 2 and 3), we present runout, areal extent, aspect ratio, and volume estimates for the four most voluminous flow units. These geometric data, combined with estimates of mass flux at the time of each unit emplacement, should be useful for future modeling efforts (Giordano and Cas, 2021).

Units I and II

Units I and II were the first of the afternoon PCs to travel across the Pumice Plain during the May 18, 1980 eruption. Where the base is exposed, Unit I is in contact with underlying debris avalanche deposits (invariably an irregular contact) and, in distal-most regions, is found in contact with underlying blast-PC deposits. Both Units I and II are predominantly fines-depleted, diffusely stratified and diffusely cross-stratified lapilli-ash in proximal to medial regions of the Pumice Plain (up to 6 km from vent; Figure 7). Pumice and lithic lenses are common and increase in size and frequency with distance from source. These deposit characteristics suggest transport and deposition under highly unsteady conditions with periods of shear stress in the flow boundary zone sufficient to promote some degree of traction transport and particle segregation. The fines-depleted nature of the deposits also suggests hindered settling conditions and the simultaneous elutriation of fine ash. Such conditions are likely the consequence of traveling across regions of variable topography and high surface roughness associated with the scattered debris avalanche hummocks.

Units I and II thicken with distance from source and grade into fines-normal to fines-enriched massive lapilli-ash (Fig. 7; Table 2), suggesting portions of the current bypassed more proximal areas to deposit distally. The massive nature of the deposits suggests a shift to more concentrated basal conditions and reduced boundary shear stress relative to upstream depositional conditions. Retention of fines suggests some degree of flow compaction (i.e., densification of the concentrated zone due to sedimentation from the upper portions of the current), hindering elutriation. Finally, a thin, massive layer of fine ash caps both Units I and II (Fig. 8), suggesting deposition through direct fallout from either the waning tail of each current or from a co-ignimbrite ash cloud. Either way, the settling of fine ash suggests a depositional pause after the deposition of both units.

Brand et al. (2014) interpret that Units I and II correlate to the early afternoon activity between 1217 - 1500. PC activity began at 1217 local time, and increased in intensity, vigor, and volume between 1220 - 1248. The activity is described as episodic, with initially buoyant masses rising through the summit crater before moving northward through the breach; this activity is described as a "pot boiling over" (Rowley et al., 1981; Criswell, 1987). It is unclear from the radio log published in Criswell (1987) how many flows were initiated or how long each current lasted. However, it is clear that a column of co-ignimbrite ash rose from the Pumice Plain 4-7 km north of the volcano at 1407. Episodic PC activity to the north continued between 1430 - 1500; the radio log notes that the time between PCs decreased and the sizes of the flows increased during this period.

Brand et al. (2014) interpreted Unit I to represent activity between 1217 - 1407, and Unit II to represent activity between 1430 - 1500. Both periods correlate with vent mass flux estimates of 3.9×10^6 kg s^{-1} (Fig. 3). Interestingly, despite the observations that numerous flows reached the North Fork Toutle Valley and Spirit Lake during this time, there are only two recognizable flow units; the sharp upper contact of each with the overlying flow unit and the fine ash layer capping Units I and II are evidence for a break in deposition. It is thus likely that both flow units are an accumulation of multiple PCs with amalgamated flow contacts. Depending on how closely spaced PC pulses were at the vent, it is also possible that PCs were locally sustained within the depositional regions of the aggrading current(s) -- that is, the depositional system of the current at any given location responds slower than fluctuations at the vent. The combination of eruption observations and deposit characteristics provides a rare chance to argue that a single flow unit may represent deposition from multiple PCs.

Units III and IV

Units III and IV are the most voluminous and widespread deposits from the afternoon PCs and correlate with the climactic phase of the eruption (Phase IV; Figure 3). The deposits are lithic-block rich, poorly sorted ash-breccias and massive lapilli-ash. Unit III often has an erosive or sharp contact with the underlying Unit II. Lithic blocks are found at the base of the Unit III, in lithic lenses dispersed through the thickness of the deposit, or as individual blocks randomly dispersed through the massive lapilli-ash. The source of these blocks range from vent derived to locally entrained from upstream debris avalanche hummocks (Pollock et al., 2016). Pumice lenses are notably absent from Unit III, which is also fines-normal to fines-enriched across the depositional area. There is no obvious decrease in median grain size or increase in degree of sorting with distance from source (Fig. 7). These observations support an interpretation of a current concentrated enough in the flow boundary zone to suppress significant size-density segregation of

pumice and elutriation of ash, but fluidized enough to prevent imbrication of clasts and to allow travel up to 8.4 km from source.

Where the contact between Units III and IV is sharp, a (rare) massive ash layer is found capping Unit III. However, the flow unit contact is more often diffuse to unrecognizable, likely due to amalgamation at the flow contact. Lithic blocks in Unit IV are found concentrated at the base as lithic breccias, dispersed throughout the deposit, or found as lithic breccia lenses throughout the unit. Like Unit III, blocks are derived from both the vent and locally entrained from hummocks (Pollock et al, 2016). Unit IV typically fines both upward and with distance from source and transitions into a massive lapilli-ash with decreasing lithic block content (Fig. 7). Coarse lapilli pumice lenses are well-developed and increase in abundance with distance from source. The massive nature of Unit IV indicates a concentrated flow boundary zone dominated by rapid sedimentation and low shear conditions; however, lateral grading of blocks and pumice lenses indicates density segregation was more efficient relative to Unit III.

The climactic phase of the eruption (Phase IV) occurred between 1500 - 1715, producing the most voluminous PCs of the afternoon. While Phase III PCs were episodic, Phase IV PCs were more continuous (Criswell, 1987). PCs flowed to Spirit Lake at 1501; PC activity increased between 1511 and 1521. During this time, PCs flowed through the breach and along the northwest and northeast flanks of the volcano, extending to Spirit Lake and the North Fork Toutle River Valley. However, between 1525 and 1600 PCs engulfed the entire north, east, and west sides of the upper volcanic slopes, although flows along the east and west only flowed several 100's of meters downslope. PC activity waned between 1605 and 1620, during which time the central column increased in vertical acceleration (Criswell, 1987). PC activity ceased by 1635, and by 1700 the Plinian column was fully re-established.

Brand et al. (2014) interpret that both Units III and IV correlate with PC activity during this time (Fig. 3), with vent mass flux estimates of 4×10^7 kg s^{-1}. The lithic block-rich nature of Units III and IV is consistent with vent widening and the increase in mass flux noted during this time. Although the 'boiling over' style PCs were more sustained and the time between flows decreased during this phase, observational evidence again suggests multiple PCs flowed northward across the Pumice Plain. However, only flow Units III and IV are correlated with this time window, again suggesting that a single flow unit likely resulted from multiple currents. The variability in deposit thickness across the depositional area is likely a consequence of currents with multiple flow paths converging along the northwestern side of the Pumice Plain (see flow lines in Figure 6), resulting in repeated units (Brand et al., 2014).

Unit V

Unit V is found across the surface of the Pumice Plain as a series of meandering, cross-cutting pumice lobes and levées. The unit extends up to 6.5 km from the vent and appears to have been deposited in a back-stepping fashion, presumably as current energy waned. Unfortunately, given the lack of cross-cutting exposures, it is not possible to see contacts between lobes and levées. Unit V is interpreted as consequence of the final PCs generated during Phase V of the eruption (Fig. 2h and 3).

Geometric Data:

We estimated the volume of Units I - IV by manually tracing isopachs of deposit thickness in 2 m intervals from measured stratigraphic sections (Supplemental Materials). The zero isopach is at the terminus of each flow unit, as best we could map given exposures. Because our volume estimates rely on measured stratigraphic sections, our estimates do not include inner crater deposits where we do not have stratigraphic sections to reference. For each unit, we calculate average thickness, equivalent runout distance (the radius of a circle of equivalent area), equivalent diameter (diameter of the circle with area equivalent to that of the PC deposit areal extent), and aspect ratios (average thickness divided by equivalent diameter) (Table 3). Volume estimates are consistent with Plinian PC deposits generated by partial to total collapse of single vent eruption columns (see Fig. 8 of Giordano and Cas, 2021), which is confirmed by eyewitness observations of the 1980 afternoon PCs (Criswell, 1987). The increase in dispersal observed from Units I and II to Units III and IV (Supplemental Materials and Table 3) corresponds to an increase by one order of magnitude in mass flux (Fig. 3), which is a first order characteristic of both dilute and dense currents for which power law relationships exist (Shimizu et al. 2019; Roche et al. 2021; Calabrò et al 2022). These geometric data, combined with estimates of mass flux at the time of each unit emplacement, should be useful for future modeling efforts (Giordano and Cas, 2021).

PC Transportation, Erosion, and Sedimentation Processes

This section combines interpretations of deposit characteristics from the afternoon PC deposits with analytical and experimental studies to address the questions (1) *What is the influence of topography on PC behavior and erosive capacity*, and (2) *What insights can we gain about PC transportation, erosion, and sedimentation processes from the combination of field observation and experiments?* We also extend the findings from the MSH case study to general PC transport and emplacement mechanisms through comparison with PCs at other volcanoes.

Influence of slope on PC behavior – PC momentum, energy, and carrying capacity

Northwest Flank: Field evidence within the Pumice Plain indicates that PCs during the climactic phase of the eruption, which deposited Units III and IV, traveled along two flow paths: portions of the currents flowed through the main breach and through the stairsteps, whereas other portions of the currents simultaneously flowed along the northwest flank (Brand et al., 2014; Zrelak et al., 2020). Repeated flow units for both Units III and IV appear within the boxed region of Figure 6. Stratigraphic correlations show that deposits originating from currents that traveled along the northwest flank contain larger lithic blocks relative to those that flowed through the breach. Pollock et al. (2016) confirms that these blocks originated from the vent, not from flank erosion. These results suggest two things that help us address the question of *topographic influence*, in particular slope: (1) currents traveling along the steep northwestern flank were not erosive, and (2) the steeper flank and more direct (shorter) flow paths allowed the currents to maintain momentum, energy, and carrying capacity relative to those that simultaneously flowed along the breach and stairsteps.

Influence of slope on PC behavior – PC transport, erosion, and sedimentation dynamics

Northeast Flank: PCs along the northeast flank, which correlate to Pumice Plain Units I-IV, were initially funneled through a narrow chute with a 30° slope (Figs. 6; Brand et al., 2016). As PCs

exited the chute they spread across the rugged northeastern flank, traveling across and through slot canyons and rugged terrain that sloped ~23°. The slope gradually decreases toward the base of the edifice to 10°, and finally down to ~5° across the northeastern Pumice Plain (Fig. 6). Perhaps it is not surprising that the northeast flank deposits differ greatly from those found within the Pumice Plain with respect to deposit characteristics (facies), but interestingly, not so much with respect to grain size characteristics (Fig. 7).

Deposit characteristics, which grade from strongly cross-stratified lapilli-ash dominated by 10s-of-meter-waveform dunes along the steep slopes to massive lapilli-ash along shallow slopes, indicates changes in particle transport mechanism as a consequence of spreading along a steep slope (Fig. 9). Brand et al. (2016) interpret that spreading and acceleration of a concentrated current along the steep upper slopes thinned the basal region of the current such that shear from the overriding, dilute, turbulent current strongly influenced the flow boundary zone. Evidence for erosion in the form of truncated bedforms and steep backset beds indicates that turbulent eddies swept through the basal region, intermittently eroding into the otherwise aggrading pyroclastic deposit (Fig. 9). The authors interpret these features as indicative of current inflation through mixing with ambient air, which is enhanced in an accelerating flow (Bursik and Woods, 1996), and autofluidization (Chédeville and Roche 2014), where air is ingested along the base of the current traveling through slot canyons and across meter-scale topographic drops.

Despite the presence of bedforms, the internally massive nature of the deposits above erosive contacts and granulometry are consistent with concentrated flows (Fig. 7), suggesting that a concentrated and at least partially fluidized flow boundary zone persisted. This is further supported by the evidence and nature of erosion by the currents. The PCs that traveled along the steep flank plucked lapilli- and block-sized clasts from the upstream slot canyon where Castle Creek Andesite bedrock and rubble are exposed (Brand et al., 2016). Roche (2015) demonstrates that dilute PCs are typically only capable of entraining particles up to 10-15 cm in size. Therefore, the entrained lithic clasts found along the mid- to upper-flank, many of which are larger than 15 cm, further indicate a concentrated flow boundary zone. Because the flow is inferred to have a dense basal region, the maximum size of entrained lithic clasts is a function of a local upward directed pore pressure gradient (Roche et al., 2013), which is directly related to the flow front velocity. Combining the formulas presented in Roche et al. (2013) and Roche (2015) with measurements of the largest locally entrained blocks found in the proximal bedded deposits, Brand et al (2016) estimated *minimum* flow front velocities of 4-6 m s^{-1} for the PCs at the site of erosion.

Brand et al. (2016) also find that bedform amplitude, wavelength, and presence of regressive bedforms and steep backset beds increase with increasing slope and with proximity to source. These features suggest that bedform morphology is related to current velocity, and perhaps to its Froude number (i.e. the ratio between the flow velocity and the velocity of surface or internal gravity waves) as well. However, interpreting bedforms with respect to supercritical conditions remains controversial (Douillet, 2021).

Given the evidence for a concentrated basal region, the experiments of Smith et al. (2020), which simulated dense, partially-fluidized, granular currents, may be more reasonable analogues for the concentrated PCs responsible for the flank deposits than the recent work on dilute PCs (i.e., Brosch and Lube, 2020; Douillet, 2021; Brosch et al., 2021). The Smith et al. experiments produce similar bedform features, including steep backset bedforms and downstream facies transitions from

bedded to massive deposits. The authors argue that the steep backset bedforms occur when currents experience a rapid deceleration and an apparent 'hydraulic' jump, which they term a 'granular jump' due to the dense, granular nature of their currents. Rapid deposition preserves the steep backset beds, in some cases up to 90°, which is consistent with what we observe within the MSH flank deposits (Fig. 9a & 9b). Moreover, their experiments produce an upstream migrating 'granular bore', which creates and preserves a series of steep backset beds remarkably similar to those observed along the MSH flank. Thus, bedforms and steep backset beds are not necessarily attributes of dilute PCs, but rather can form in a wide range of granular concentration regimes.

The gradual, downslope transition from cross-stratified to massive deposits indicates a thickening of the flow boundary zone due to suspension sedimentation from the overriding current (Brand et al., 2016). The massive deposit characteristics suggest that the flow boundary zone of the currents along shallow slopes were concentrated, fines-rich granular flows with elevated pore pressures (Figs. 6 and 9). Such variations indicate that slope has a significant influence on PC dynamics, with the lateral grading of deposit characteristics revealing the morphodynamic nature of PCs.

Elevated gas pore pressure during transport and mixing at the flow-bed interface

The mobility of the afternoon PCs, which allowed them to transport and deposit up to 8 km from source while maintaining a matrix of fines, suggests elevated gas pore pressure in the flow boundary zone up to the distal reaches of the Pumice Plain (Brand et al., 2014). Further, the work of Rowley et al. (1981) presents evidence that elevated gas pore pressure persisted for days post-deposition, including (1) the quicksand-like nature of the deposits, (2) reports that a rock tossed onto the PC deposit surface caused "splashes and waves and tiny jets of air to escape from the surface", and (3) that deflation of the surface by up to 1 m or more occurred in the days following the eruption. It is likely that the low permeability of the deposits led to both the initial trapping of the gas and the slow diffusion of gas out of the deposits in the days following the eruption.

Further, recumbent flame structures, where material from an underlying PC deposit protrudes into an overlying deposit but bends and extends in the downstream direction before tapering to a point and pinching out (Fig. 10; Brand et al., 2017; Pollock et al., 2019), are further evidence for elevated gas pore pressures. These structures are found throughout Units I-IV. Because of how fluid-like the mixing structures appear, Pollock et al. (2019) assert that both the basal zone of PCs and the uppermost part of the deposits must themselves have fluid-like properties prior to and during mixing, perhaps forming via processes similar to Kelvin-Helmholtz instabilities that occur in pure fluids (Rowley et al., 2014; Farin et al., 2014). This observation lends further credence to the presence of elevated gas pore pressure in both the basal part of the flow and the substrate to enable fluid-like mixing (e.g. Girolami et al., 2015). These structures additionally indicate high particle concentrations in the lower-flow boundary zone; otherwise, the elongated tails of the structures would collapse back to the bed rather than being preserved in the deposits (Brand et al., 2017; Pollock et al., 2019).

To investigate what quantitative information might be extracted from recumbent flame structures, Pollock (2019) expanded the investigation of Rowley et al. (2011) to experimentally investigate the influence of the amount of pore pressure in granular flows, grain size of the substrate, and slope angle on the formation and evolution of recumbent flame structures (Fig. 10d-10f). Pollock shows that higher pore pressure in the flow promoted more efficient mixing at the flow-bed interface He also showed that both the length and height of the experimentally created recumbent flame

structures scaled with the flow front velocity regardless of bed conditions (slope angle or grain size). Pollock (2019) extracted scaling relationships from the experimental results that relate the length and height of the recumbent flame structures to the flow velocity and flow height, respectively. Since the aspect ratio (length vs height) of both experimental and natural structures are well-correlated, despite a variation in size of almost 5 orders of magnitude (R^2=0.96), Pollock (2019) argues that the instability growth criterion and scaling relationships developed from experiments can be applied to extract quantitative information about the PCs responsible for the formation the recumbent flame structures at MSH. He found minimum basal slip velocities that range from 0.2 m s^{-1} for the smallest structures (only a few cm long; Fig. 10a) to 7.5 m s^{-1} for the largest structures (more than 30 m long; Fig. 10c). Further, combining the estimates for basal slip velocities with the morphology of the recumbent flame structures (the length of the tail provides a timescale for deposition), the smallest structures indicate deposition rates of 4 cm s^{-1}, and the largest structures indicate deposition rates of 32 cm s^{-1}.

Particle segregation and shear in the flow boundary zone

The deposit textural characteristics, componentry, and particle alignment also provide insight into the conditions and processes in the flow boundary zone that lead to the segregation of particles according to their size and density. Observations of vertical and lateral facies variations throughout the Pumice Plain deposits demonstrate efficient density segregation in PCs associated with the climactic phase of the eruption (Brand et al., 2014). The occurrence of pumice lenses in Units I, II, and IV increases with distance from the vent suggesting that segregation processes become more efficient over the duration of PC transport. Segregation not only occurred for the low density pumice, but Unit IV also demonstrates efficient density segregation and the development of lithic-rich lower flow boundary zones that deposited numerous basal lithic breccias (Brand et al., 2014). Further, well-developed pumice levées and snouts on surficial PCs deposits (Unit V) were obvious immediately after the eruption and demonstrated efficient segregation of large, low density pumice clasts to the fronts and lateral margins of late, smaller-volume PCs during the depositional stage (Wilson and Head, 1981). In contrast, the lack of pumice lenses in Unit III, which is also fines-normal to fines-enriched across the depositional area with no discernable decrease in median grain size or increase in degree of sorting with distance from source (Fig. 7), suggest a current concentrated enough in the flow boundary zone to suppress significant size-density segregation of pumice and elutriation of ash, but fluidized enough to allow the PCs to travel up to 8.4 km from source.

Sequential fragmentation/transport theory (SFT) predicts the mass distributions of components based on the physical principles of fragmentation and transport (Wohletz et al., 1989). The method constrains the relationship between particle segregation with transport conditions. Application of this fine-scale approach to the deposits at MSH by Mackaman-Lofland et al. (2014), who explored the variation in the distribution of pumice, vitric glass fragments, accidental lithics, and free crystals across multiple grain sizes with distance from source for a range of different facies (e.g., massive lapilli ash, ash breccias, cross-stratified deposits), demonstrates the importance of density segregation across the entire depositional region. Their analysis suggests that density segregation acts equally on low density portions of the current (i.e. pumice lenses) as well as high density regions (i.e. basal lithic breccias), which corroborates the outcrop scale observations mentioned above (Wilson and Head, 1981; Brand et al., 2014). SFT analysis also revealed that particle-density

relationships are reflective of regional transport conditions rather than localized (outcrop-scale) variations due to current unsteadiness or interaction with high surface roughness.

Particle size segregation is interpreted as evidence for elevated shear rates within the depositional region of PCs (Branney and Kokelaar, 2002), which is further supported by a number of experiments that demonstrate how high shear rates promote segregation processes (Johnson et al., 2012; Fan and Hills, 2015; Xiao et al., 2016). Additional evidence for shear in the flow boundary zone includes particle orientation (Capaccioni and Sarocchi, 1996; Hughes and Druitt, 1998; Valentini et al., 2008). Measurements of particle orientations (i.e. particle-shape fabric) within the PC deposits demonstrate the development of strong preferred particle orientations. Particle shape-fabric studies at MSH indicates that shear in the lower-flow boundary zone is sufficient to produce mutual alignment of elongated particles in the dominant shearing direction (i.e. in the direction of dominant transport, Zrelak et al., 2020). However, particle orientation can vary vertically within a deposit by almost 90 degrees, which the authors interpret is the effect of variations in the dominant shearing direction over short spatial scales and timescales or that elongated particles rolled with their longer axis perpendicular to the flow. Such fine-scale variability within a single outcrop also reflects local current unsteadiness and suggests step-wise aggradation (Zrelak et al., 2020).

The erosive nature of PCs – Self-channelization

Self-channelization occurs when a current erodes the underlying substrate and creates a channel, resulting in confinement or partial confinement of the body of the initially erosive current. Brand et al. (2014) report evidence for large-scale self-channelization within Units III and IV in the form of a large scour and fill deposits (Fig. 11a and b). Investigating the extent of these features using ground penetrating radar (GPR) imaging reveals two broad channel scour and fill features (Gase et al., 2017), both oblique to the direction of increase in slope from 5° to ~15° along the central to northwest area of the Pumice Plain (see black arrow in Figure 6). The northern channel is ~12 m deep, >200 m wide, and at least 500 m long; the southern channel is ~15 m deep, ~400 m wide, and also at least 500 m long. These channels, which are morphologically similar to incipient scours or broad megaflutes carved by turbidity currents (Elliott, 2000; Fildani et al., 2013), are the largest PC-derived scour and fill features identified in the world.

Both channels begin where the PCs turn from northward to northwestward along the increased slope gradient. Since the base of each scour appears at the contact with the underlying unit, erosion most likely occurred during the passing of the current head. Erosion by the PC head is consistent with experimental studies on fluidized granular flows, which demonstrate that the sliding head of a current generates both shear and an upward pressure gradient whose combined effects enable erosive capacity (Roche et al., 2013). As discussed above, the fluidized nature of the underlying deposits likely further facilitated erosive capacity (Brand et al. 2014). Finally, the lack of buried hummocks or other topographic irregularities, combined with the initiation of scouring where the slope increases, indicate that the increased slope angle was likely the primary driver for scouring in this specific location.

Gase et al. (2017) estimate 1.6×10^6 m^3 of material was removed from both channels before they filled by the aggrading body of each current. While the consequences of such erosion to current dynamics are not clear from the deposits alone, Gase et al. (2017) postulate that such extensive erosion certainly would influence current dynamics, likely by increasing the runout distance due to increasing the density contrast with the atmosphere. However, it is equally possible that erosion

extracted momentum, perhaps driving quicker downstream deposition. Experimental studies are necessary to understand the consequences of large-scale erosion.

We also know from numerical modeling that channelized currents have longer runout distances than PCs spreading across a flat plain (Dufek, 2016), while turbidity current experiments reveal increased longitudinal flow velocities along the axis of confined channels (de Leeuw et al., 2016). Thus, channelization of the PC body and subsequent flows within the channel would likely increase the velocities and carrying capacities of those currents, which is further evidenced by the presence of outsized, vent-derived accidental blocks in the MSH channel fill (Figure 11a and 11b; Brand et al., 2014; Pollock et al., 2016). Thus, while the full impact on runout distance and PC dynamics is not decipherable from the deposits alone, it is likely that the runout distance of the channelized currents would increase by maintaining velocity, energy, and carrying capacity within the channel-confined area.

The erosive nature of PCs – Plucking of lithic clasts from substrate

Investigation of the deposits from the May 18, 1980 eruption reveals additional evidence for the mechanisms by which concentrated PCs entrain substrate material. Pollock et al. (2016) identify PC deposits containing locally entrained lithic cobbles to boulders, derived from upstream debris avalanche hummocks based on the statistical similarity of the lithic componentry (Fig. 11c). Entrained lithic clasts were found both directly above unit contacts and within the massive deposits of each flow unit, meters above the unit contact. While locally entrained material sitting just above the flow unit contact indicates erosion at the flow front followed by rapid downstream deposition, the presence of locally entrained material high above unit contacts indicates that erosional processes continue after the passing of the current head. Alternatively, such substrate erosion may indicate multiple PC pulses from the vent that are not recorded as individual flow units due to amalgamation of flow contacts, which is supported by the visual observations described earlier in the paper.

Experiments on erosional processes in granular flows indicate that plucking of individual boulders from the debris avalanche hummocks likely occurs as a result of both shear and an upward directed pore pressure gradient that occurs at the sliding head of fluidized granular flows (Girolami et al., 2010; Roche et al., 2013; Roche, 2015). As mentioned in the section *Influence of slope on PC behavior*, quantitative relationships derived from experiments allow for an estimation of minimum flow front velocity based on the size of locally entrained clasts. For the PC deposits containing some of the largest locally entrained clasts, Roche et al. (2013) estimate flow front velocities of 10.5–13.3 m s^{-1} and 8.9–11.2 m s^{-1} at distances of 5.6 and 7.2 km from the vent, respectively.

The main limitation of these simplified experiments is that they are conducted on uniform substrates with no complex topography while natural substrates are commonly irregular surfaces. PCs traveling across rugged or irregular terrain may experience enhanced erosion for many reasons. For example, MSH PCs traveling between debris-avalanche hummocks may have experienced local acceleration, especially through constrictions, and increased shear along the flow boundary zone and substrate interface. Because the magnitude of both shear (Girolami et al., 2010) and pressure gradient (Roche et al., 2013) are a function of flow velocity, the interaction of the PCs with the complex topography of the debris avalanche deposit likely increased substrate entrainment relative to passage across a smooth, flat topography. Shear across or undercutting of

the debris avalanche deposit is also possible and supported by the increase in the proportion of fines in PC deposits downstream from fines-rich hummocks, which suggests hummock matrix erosion in addition to erosion of blocks. Such interactions and their role in promoting erosion warrant further exploration.

Entrainment of large blocks and matrix from the debris avalanche deposit into the PC body or re-entrainment of the aggrading PC deposit likely has significant effects on overall flow behavior due to the addition of mass and fine ash to the flow boundary zone. However, the impact of such erosion is not discernable from the deposits alone. As such, next we turn to additional experiments to better understand the consequences of erosion on PC dynamics.

Consequences of substrate erosion – Beyond MSH

Complementary studies of MSH PC deposits and experimental work provide insights into both the conditions that promote substrate erosion (i.e., presence of gas pore pressure in the aggrading deposit, slope angle, surface roughness) and the physical processes by which PCs entrain bed material (i.e., mixing at the flow-bed interface, shear, pressure gradient). However, the MSH PC deposits do not record the *consequences* of substrate erosion on PC behavior or runout distance. For this, we must go *beyond* MSH and consider a number of recent studies that shed light into both the causes and consequences of erosion.

Recent research demonstrate that, under certain conditions, the characteristics of the bed will extend the runout distance of both fluidized and dry granular flows traveling across inclined slopes (Mangeney et al., 2010; Farin et al., 2014; Chédeville and Roche, 2014; 2015). For example, the authors specifically mention that increased runout distance cannot be explained only by the increase in flow mass associated with erosion (Farin et al., 2014). Instead, following initial acceleration and then deceleration, flows enter a late slow propagation phase that is extended by the presence of an erodible substrate. The increased duration of the slow propagation phase ultimately allows for increased runout distances (Farin et al., 2014). However, the causes of this late phase propagation are elusive and could be the focus of future research. A complementary study by Chédeville and Roche (2014; 2015) identified a process termed ‘autofluidization’ for the increased runout distance of flows traveling over a rough, fixed bed made of a layer of particles glued to the base of the flume. When particles fall into the interstices between substrate particles, interstitial air is expelled upwards into the overriding flow. The flux of air into the flow effectively extends the timescale for defluidization and results in increased runout distances compared to flows traveling over a smooth bed. In nature, this mechanism can operate along with flow compaction or deflation (Breard et al. 2018) to generate sustained high pore pressure.

Other recent studies indicate that the relationship between erosion and runout distance may not be so straightforward (Iverson et al., 2011; Pollock, 2019). Using experimental configurations that closely resemble those of Chédeville and Roche (2014; 2015), Pollock (2019) observed a decrease in the runout distance of fluidized granular flows that travel over a thick (i.e., bed thickness greater than the flow thickness), erodible bed relative to those that travel over a fixed, non-erodible bed of particles. The decreased runout distance in the case of the thick, erodible bed is attributed to the downward diffusion of pore fluid pressure into the granular bed (cf. Major 2000) and thus more rapid defluidization. Thus, while evidence for substrate erosion by PCs abound at MSH and many other locations (e.g., Buesch, 1992; Cole et al., 1998; Calder et al. 2000; Bernard et al., 2014), the

consequences of substrate erosion on PC behavior and runout distance remain enigmatic, and is perhaps one of the least understood aspects of PC dynamics.

Boil-over PC Summary

The combination of eruption observations, including number of currents produced during different eruptive phases and their emplacement timing, coupled with stratigraphic mapping of units, highlights that a single flow unit may represent deposition from multiple PCs. The studies described above also demonstrate the importance of deposit mapping, including facies characterization, granulometry and componentry studies, and deposit geometric properties for constraining conditions in the flow boundary zone and that of the aggrading deposit. For example, studies at MSH show that steep slopes allowed PCs to maintain momentum, energy, and carrying capacity relative to those that simultaneously flowed along the breach and stairsteps. The presence of bedforms along the steep flanks, which grade into massive deposits as the slope shallows, attests to the morphodynamic nature of PCs in response to topographic changes and surface roughness. We also find that an increase in slope angle can trigger scouring of channels by the current head. Outsized, vent-derived accidental blocks filling these channels indicate that channelization of the PC body and subsequent flows increases the carrying capacity of those currents.

The combination of field and experimental studies highlights the importance of gas pore pressure on controlling flow dynamics and runout distance. Such work also demonstrates some degree of shear between the flow boundary zone and aggrading deposit, evidenced by the presence of recumbent flame structures, particle shape-fabric in the dominant shearing direction (i.e. in the direction of dominant transport), and the plucking of accidental lithic blocks from debris avalanche hummocks.

The work presented herein also highlights the importance of coupling empirical relationships from scaled experiments with deposit characteristics to lend insight into current dynamic conditions at the time of deposition, including the possibility of extracting properties such as flow front velocity, basal slip rates, and deposition rate. For example, experiments on erosional processes in granular flows indicate that plucking of individual lithic blocks from the debris avalanche hummocks likely occurs as a result of both shear and an upward directed pore pressure gradient that occur at the head of fluidized granular flows. Quantitative relationships derived from experiments allow for the estimation of minimum flow front velocity based on the size of these locally entrained clasts.

June, July, and August 1980 PCs

Of the PC deposits from the post-May 18, 1980 eruptions, only those of June 12 and July 22 remain well-preserved. PCs generated during the June 12, July 22, and August 7 events were well documented photographically and carefully studied prior to their partial or complete destruction in the winters of 1981 and 1982 (Table 1; Kuntz et al. 1990, Rowley et al. 1981). Here we focus on these eruptions and the PCs they produced, disregarding other post-May 18 eruptions whose PC deposits were destroyed before an adequate study could take place.

Observations and geophysical data indicate that the June, July, and August eruptions occurred as discrete events that produced single pulse PCs. Weather and darkness obscured the eruptions on June 12; however, seismicity indicates that PCs began at 2111 local time and continued sporadically for several hours (Seth Moran, written communication, 2022). Field mapping

indicates that only two PCs were voluminous enough to reach the Pumice Plain (Vallance, et al., 2017). The well-observed eruption of July 22 included three explosive events (Table 1). The first of these at 1714 PDT ruptured the pre-existing dome but did not form significant PCs. The second and third explosive events at 1825 and 1901 PDT both generated PCs that emerged from the open crater (Fig. 12), descended the steep terrain of the stairsteps, and spread out onto the Pumice Plain (Rowley et al., 1981). Each of these currents were in motion for approximately 10 minutes before coming to rest (Hoblitt, 1986). The deposit of the second event was entirely in place before the PC generated by the third event overran it. The eruption of August 7 consisted of a single explosive event that generated a PC. The PC descended the steep slopes of the stairsteps and spread out on the upper reaches of the Pumice Plain. From inception to emplacement, the current was in motion for 6.5 minutes (Hoblitt, 1986).

The PC deposits of June, July, and August 1980 consist of levée-channels and frontal lobes with complex overlapping relationships (Vallance et al., 2017). Lobe termini and outer levées are coarser grained, richer in pumiceous blocks and coarse lapilli (of various densities), and more pumice-rich than channel deposits, which have comparatively higher concentrations of ash-size grains. Although deposit-surface morphologies appear complex, they suggest that individual PCs shared common traits (Vallance et al., 2017). First, analysis of oblique and aerial photography indicates the PCs were widely spread initially, then became progressively more confined, levéed, and lobate as they traveled across the shallow-dipping Pumice Plain (Fig. 13). Second, along established paths the PCs formed multiple sequences of nested levées with some having a dozen or more levée pairs (Fig. 13). Third, as the PCs came to rest, they formed cauliflower-shaped termini consisting of successively emplaced coarse-grained granular lobes that indicate deposition from a succession of pulses (Fig. 13).

The concentration of coarse lapilli and blocks in deposit lobes and levées, roundedness of coarse grains, and an ability of the currents to carry large pumiceous and lithic blocks several kilometers across low gradients indicates the post-May 18 PCs that traveled across the Pumice Plain behaved as partially fluidized granular flows but with strong frictional and collisional particle interactions at their margins. In particular, deposits that include lobes and levées with marginal concentrations of coarse lapilli and blocks imply a frictional granular flow regime in which coarse particles are segregated and migrate toward current margins (Fig. 14). The segregation process begins with migration of coarse and low-density lapilli and blocks upward through the flow boundary zone until they reach the top of the concentrated portion of the current. Here, these coarse-grained clasts move faster than the average velocity of the current and therefore migrate to both lateral and frontal flow margins where they accumulate to form levées and a lobe, respectively (Fig. 14; Johnson et al, 2012). The coarse levées lack fines, which enhances pore pressure diffusion and favors frictional interactions and deposition. In contrast, the portions of the currents between levées remain fines-rich and are interpreted as fluidized during emplacement (Kokelaar et al., 2014). After passage of PC fronts, the more-fluid, fines-rich flow interiors drain away and the center of the channel becomes progressively lower than that of the lateral levées. As the flow interior drains away, marginal deposits are undermined and collapse progressively from the inside outward toward levée margins in a process that Kokelaar et al. (2014) term levée sharpening.

Overlapping lobes exist for each PC event, despite individual PCs being generated by simple, one-pulse events at the vent. This overlap indicates that PCs broke into waves or became pulsatory as they moved onto and across the relatively shallow surface of the Pumice Plain (Vallance et al.,

2017). Experimental studies show that steady granular flows on an incline commonly develop surface-wave instabilities (Pouliquen and Vallance 1999) even at Froude number less than one (Forterre and Pouliquen 2003), and pulsating behavior is common in stratified PCs (Brosch et al., 2021). In this regard, the post-May 18 PCs at MSH were prone to surface instabilities regardless of their source conditions because they were likely (partly) fluidized and had Froude numbers greater than one based on Hoblitt's (1986) observations of the August PC velocities and plausible estimates of thickness of the dense phase of the current (Vallance et al., 2017).

Polydisperse granular flows are known to experience a phenomenon called granular fingering (Pouliquen et al. 1997), which is related to the emergence of front instabilities that grow as the material propagates downslope to form a series of parallel secondary flows (or fingers). These fingers are typically characterized by coarse-rich frontal lobes and lateral levées. Simple laboratory experiments show that the granular fingers may be adjacent or separate from each other depending on the degree of polydispersity and the proportion of coarse particles (Valderrama et al. 2018). However, the field evidence observed in the post-May 18 PC deposits, which have complex, overlapping relationships within individual PC units, is inconsistent with the fingering hypothesis. Instead, field relationships support a succession of waves propagating down channel, encountering resistance to flow then breaking out in a rapid sequence of lobes first in one direction then another.

In summary, the evidence presented herein indicates that the post-May 18 PCs were sufficiently concentrated as they crossed the Pumice Plain to behave as free-surface, partly fluidized granular flows subject to surface-wave and flow-front instabilities and particle-size segregation to form a complex succession of levéed-channels and lobes.

Temperature measurements of the 1980 MSH PC deposits and their significance

The 1980 explosive eruptive sequence at MSH led to several pioneering temperature studies (Fig. 15). The objective of these studies was to establish emplacement temperatures of PC deposits across their areal extent, which provides information for understanding PC generation, transportation, and deposition.

Within days to months after the paroxysmal eruption of May 18, 1980, a group of USGS scientists began an extensive campaign of direct temperature measurements of the PC deposits (Moore and Sisson, 1981; Banks and Hoblitt, 1981; 1996). These studies found that the debris avalanche was emplaced at low temperature (<100°C), whereas blast-PC deposit was emplaced at slightly higher temperatures (100-300°C). The authors interpret that cooling of the blast-PC resulted from extensive entrainment of ambient air during the PC formation.

The PC deposits that followed from May 18 through October 17 were progressively hotter, with emplacement temperatures ranging from about 300 to 730°C, reaching up to 850°C in vent facies. Individual flow units exhibited little temperature change with distance from the vent despite traveling over a relatively complex terrain. Thus, temperature variations across the PC sequence from May to October were attributed to variations in the "eruption vigor"; that is, most heat transfer occurred near the vent during fountain collapse processes and/or at the start of the lateral flow rather than along subsequent PC propagation.

Paterson et al. (2010) applied paleomagnetic methods on lithic clasts preserved in some of the 1980 PC deposits. Their data are in good agreement with the direct measurements of Banks and Hoblitt (1996), illustrating the accuracy of the paleomagnetic method for estimating emplacement temperatures. Bowles et al. (2018) used similar techniques to study the emplacement temperatures of the May 18 PC deposits. They also found temperatures similar to those retrieved by Banks and Hoblitt (1996) and highlighted that temperature variations are also observed across different PC units of the more voluminous May 18 deposits.

We extended paleomagnetic measurements from proximal to distal regions across different flow paths and paleo-topography to investigate the impact of irregular topography on the dynamics of the May 18 PCs by coupling emplacement temperature estimates with three-dimensional multiphase numerical models (see data repository, Trolese 2022). We found emplacement temperatures that are in excellent agreement with the measured values from previous authors. Our data show that the average emplacement temperature along the northeastern flow path was about 100°C higher than flows that descended the stairsteps channel on the northwestern flank (Fig. 15). In contrast, emplacement temperatures on both flow paths remained approximately uniform with distance from the vent. Numerical simulations demonstrate that the presence of major topographic irregularities (i.e., stairsteps) lead to local thermal expansion of the body and strong vertical ingestion of air, which may also affect the basal region of the current reducing the emplacement temperature and final runout distance.

In the absence of major topographic obstacles and/or significant ingestion of cold external material, evidence for conservation of heat along PC flow paths (e.g., Lesti et al., 2011; Porreca et al., 2008; Trolese et al., 2017; 2018; Giordano et al., 2018) implies that air entrainment at the head and edges of the PC may not appreciably affect the inner high concentration depositional system. Instead, the effects of cooling by air entrainment may be limited to the suspended load in the upper part of the current (Pensa et al. 2019). Trolese et al. (2019) extends this work to explore and quantify the role of air entrainment in promoting rapid cooling of the ejected mixture that eventually forms PCs. They find that initial PC temperature is linearly correlated with the percentage of collapsing mass (i.e., the ratio between the total mass collapsing rate and the mass eruption rate at vent), with partial collapse regimes entraining significant amounts of air to generate cooler PCs. Thus, the progressive increase in temperature observed in PC deposits of May, June, July, August, and October is herein interpreted to reflect an increase in the ratio between the mass flux feeding the currents and total mass erupted. Initial magma temperatures and the percentage of column collapse, caused by variations in the vent conditions (e.g., an increase of crater radius or a decrease of total volatile content in the eruptive mixture), may also have played a role.

Conclusions

The well-exposed and well-preserved PC deposits from the 1980 eruption sequence at MSH continue to provide a natural laboratory to improve our understanding of eruption dynamics and volcanic hazards. This review summarizes what we have learned thus far from studying pyroclastic current (PC) deposits from the 1980 eruption sequence and provides the volcanology community with questions that can be addressed as our field, experimental, and numerical research techniques advance.

A combination of visual observations, damage patterns, deposit characteristics, and multiphase numerical modeling indicates that the MSH blast-PC was a gravity-driven density current. Rapid decompression of a partially crystalized cryptodome provided the mechanism for magma fragmentation and initial lateral acceleration of the gas-particle mixture. Collapse of the expanding, dense, fragmented mixture produced a blast-PC with a leading, high shear, high velocity turbulent front that facilitated substrate erosion, followed by a stratified sedimenting body. The highest dynamic pressures, and thus damage, were associated with the turbulent head of the current. The dynamics of the MSH blast-PC were influenced, but not controlled, by topography.

With respect to the afternoon boil-over PCs, our summary shows that coupling visual observations of the eruption, field data (deposit mapping, stratigraphy, and facies analysis), laboratory studies (granulometry, componentry, and particle-shape fabric), and fluidized granular flow experiments provides substantial insight into PC dynamics. In particular, the combination of approaches allows researchers to evaluate the influence of surface roughness and topography on PC behavior, the prevalence, causes, and consequences of substrate erosion by PCs, and insights into the PC transportation and sedimentation processes. The work summarized herein shows that a single deposit unit may represent deposition from multiple PCs and that topography has a strong control on concentrated PC dynamics and erosive capacity. Erosion occurs across a wide range of scales (i.e., plucking of individual clasts to self-channelization), and entrained substrate material is found near the flow basal contacts and well above flow contacts indicating that erosion occurs both with the passing of the initial current head and within the body of a current. Empirically derived relationships from fluidized granular flow experiments can be applied to certain deposit characteristics, namely recumbent flame structures and the size and density of eroded lithic clasts, to extract conditions at the time of emplacement, such as flow front velocities, basal slip rates, deposition rates, and relative concentration in the depositional region of a current. However, additional research is necessary to investigate PC dynamics and in particular the flow boundary zone and the aggrading deposit interface as a function of internal pore pressures (of the flow and aggrading deposit), as well as the causes and consequences of substrate erosion.

Post May 18 explosive eruptions at MSH generated pumiceous PCs as a result of discrete explosive events; PCs from these discrete explosions were in motion for a few minutes to a few tens of minutes at most, producing overlapping deposits with levée-channel and lobate morphology. These deposits are unlikely to be caused by waxing and waning of supply at the source since the eruptive events that produced them were observed to be single-pulse in character. Thus, we infer that fast-moving granular flows at relatively high slope angles in proximal domains experienced surface wave instabilities that led to successive pulses. Once the flows began crossing the shallow-dipping Pumice Plain, the successive pulses resulted in surface-wave instabilities and particle-size segregation, producing levée-channel morphologies.

Finally, temperature measurements across a wide range of PC-producing events and numerical simulations indicate that PC temperature is linearly correlated with the percentage of collapsing mass (i.e., the ratio between the total mass collapsing rate and the mass eruption rate at vent). The combination of field and numerical studies also show that concentrated flows can conserve and maintain their temperatures across their depositional extent, indicating that air entrainment along the flow is negligible and does not affect the depositional system.

Future Directions:

While we have learned much from the studies at MSH and beyond, there is much still to explore. With respect to modeling blast-PCs, the compilation of work presented herein highlights the need to reduce uncertainty in modeling the basal region of the current. Model advances could explore the development of large-scale coherent vortex structures and waves (i.e., Brosch et al., 2021), the causes and consequences of erosion, conditions influencing dynamic pressures, and how the more concentrated flow boundary zone influences deposit characteristics. Investigating initial conditions in numerical models would further constrain the effect of vent conditions on blast-PC dynamics, particularly focusing on the energy released during that fragmentation process and the emerging grain-size distribution, damage potential, and runout.

One of the understudied factors of PC generation and emplacement is the inherent role of bubble growth, fragmentation and gas release both within the vent but also during PC transport. The blast-PC originated from a complex, near-surface reservoir generated from multiple magmatic intrusions over a period of several weeks. The cryptodome experienced variable volatile loss and growth of groundmass microlite crystals (Blundy and Cashman, 2005; Blundy et al., 2008) accompanied by bubble growth and deposition of vapor-phase tridymite crystals over a period of days to weeks (Hoblitt and Harmon, 1993). Melt inclusion data indicate that the cryptodome dacite retained <1-3% water vapor before eruption (Blundy et al. 2008). The massive landslide exposed the cryptodome, causing rapid decompression that triggered a second stage of bubble nucleation (Hoblitt and Harmon, 1993), but bubble growth and coalescence may have been inhibited by the variable, but abundant micolites (Klug and Cashman, 1994). The numerical model of Esposito Ongaro et al. (2012) assumed bubble fragmentation to be instantaneous with decompression, but growth may have occurred within a few 10's of seconds after decompression during blast generation. In contrast, the afternoon, boil-over PCs originated from a reservoir $\geq$8 km depth that retained 4-7% water vapor in microlite-free glass before eruption (Blundy et al. 2008). Bubble growth occurred in response to decompression during magma ascent over a period of 30 to 70 minutes (Klug and Cashman, 1994; Criswell 2021) and created extensive bubble coalescence and high magma permeability (Klug and Cashman, 1996). Fragmentation occurred during final moments of ascent with some evidence of ductile bubble wall behavior after fragmentation (Klug and Cashman, 1994). Much remains to be studied about how these different fragmentation mechanisms and the juvenile clasts they produce influence PC dynamics, including the release of gas from pyroclasts during PC transport and the influence of juvenile clast comminution on ash properties of a current.

Finally, while there is great progress in interpreting the nature of the flow boundary zone through the combination of fluidized granular flow experiments and analysis of deposit characteristics, a quantitative criterion for a static-mobile interface, whose dynamics controls substrate entrainment and flow deposition, remains a challenge. Many questions remain regarding the nature and influence of shear, the conditions that promote substrate erosion, and the consequences of substrate erosion on PC behavior, including:

Is particle-shape fabric (particle iso-orientation) controlled by shear at the time of deposition, or shortly after deposition by remobilization by a shearing, overriding current? Further, how does particle-shape fabric (particle iso-orientation) relate to specific flow and shear conditions in the depositional zone of a PC?

What are the relative contributions of ash column fountaining (Valentine and Sweeney 2018; Fries et al. 2021), auto (or self) fluidization caused by flow deflation (Breard et al. 2018) or a rough substrate (Chédeville and Roche 2014), and degassing of pyroclasts in generating high gas pore pressure in PCs?

Can we use recumbent flow structures to constrain the degree of fluidization of the flow or substrate?

Deposit structures and bed-erosion allow quantification of flow velocity and deposition rates at basal flow boundary. How could we infer flow properties above the lower flow boundary zone?

What are the contributions of PC initiating characteristics (sustained versus discrete), volume, flow rate, granulometry, and polydispersity in controlling the difference between largely flat-topped, valley fill deposits Unit I - IV deposits of May 18, 1980, and the later flow deposits dominated by lobes and levées (e.g., Unit V from May 18 and post 18-May PCs)?

Acknowledgments:

Funding for this work was provided through National Science Foundation grants NSF-EAR 0948588 and 1347385.

References Cited

Alatorre-Ibargüengoitia MA, Scheu B, Dingwell DB, et al (2010) Energy consumption by magmatic fragmentation and pyroclast ejection during Vulcanian eruptions. Earth Planet Sci Lett 291:60–69. doi: 10.1016/j.epsl.2009.12.051

Alidibirov MA (1995) A model for the mechanism of the May 18, 1980 Mount St. Helens blast. J Volcanol Geotherm Res 66:217–225. doi: 10.1016/0377-0273(94)00065-O

Banks NG, Hoblitt RP (1996) Direct temperature measurements of deposits, Mount St. Helens, 1980-1981. US Geol Surv Prof Pap 1387

Belousov A, Belousova M, Hoblitt R, Patia H (2020) The 1951 eruption of Mount Lamington, Papua New Guinea: Devastating directed blast triggered by small-scale edifice failure. J Volcanol Geotherm Res 401:106947. doi: 10.1016/j.jvolgeores.2020.106947

Belousov A, Voight B, Belousova M (2007) Directed blasts and blast-generated pyroclastic density currents: A comparison of the Bezymianny 1956, Mount St. Helens 1980, and Soufrière Hills, Montserrat 1997 eruptions and deposits. Bull Volcanol 69:701–740. doi: 10.1007/s00445-006-0109-y

Bernard J, Kelfoun K, Le Pennec J-L, et al (2014) Pyroclastic flow erosion and bulking processes: comparing field-based vs. modeling results at Tungurahua volcano, Ecuador. Bull Volcanol 76:1–16. doi: 10.1007/s00445-014-0858-y

Blundy J, Cashman K (2005) Rapid decompression-driven crystallization recorded by melt inclusions from Mount St. Helens volcano. Geology, 33(10), 793-796.

Blundy J, Cashman KV, Berlo K, Sherrod DR, Scott WE, Stauffer PH (2008) Evolving magma storage conditions beneath Mount St. Helens inferred from chemical variations in melt inclusions from the 1980–1986 and current (2004–2006) eruptions. US Geological Survey professional paper, 1750, 755-790.

Bowles JA, Gerzich DM, Jackson MJ (2018) Assessing New and Old Methods in Paleomagnetic Paleothermometry: A Test Case at Mt. St. Helens, USA. Geochemistry, Geophys Geosystems 19:1714–1730. doi: 10.1029/2018GC007435

Brand BD, Bendaña S, Self S, Pollock N (2016) Topographic controls on pyroclastic density current dynamics: Insight from 18 may 1980 deposits at Mount St. Helens, Washington (USA). J Volcanol Geotherm Res 321:1–17. doi: 10.1016/j.jvolgeores.2016.04.018

Brand BD, Mackaman-Lofland C, Pollock NM, et al (2014) Dynamics of pyroclastic density currents: Conditions that promote substrate erosion and self-channelization - Mount St. Helens, Washington (USA). J Volcanol Geotherm Res 276:189–214. doi: 10.1016/j.jvolgeores.2014.01.007

Brand BD, Pollock NM, Sarocchi D, et al. (2017) Field-trip guide for exploring pyroclastic density current deposits from the May 18, 1980, eruption of Mount St. Helens, Washington. USGS Sci Investig Rep 2017-5022-C

Branney MJ, Kokelaar BP (2002) Pyroclastic Density Currents and the Sedimentation of Ignimbrites, Issue 27. Geological Society of London

Brantley SR, Waitt RB (1988) Interrelations among pyroclastic surge, pyroclastic flow, and lahars in Smith Creek valley during first minutes of May 18, 1980 eruption of Mount St. Helens, USA. Bull Volcanol 50:304–326. doi: 10.1007/BF01073588

Breard ECP, Dufek J, Lube G (2018) Enhanced mobility in concentrated pyroclastic density currents: An examination of a self-fluidization mechanism. Geophysical Research Letters 45:654–664, https://doi.org/610.1002/2017GL075759

Breard ECP, Dufek J, Fullard L, Carrara A (2020) The Basal Friction Coefficient of Granular Flows With and Without Excess Pore Pressure: Implications for Pyroclastic Density Currents, Water-Rich Debris Flows, and Rock and Submarine Avalanches. J Geophys Res Solid Earth 125:. doi: 10.1029/2020JB020203

Breard ECP, Jones J, Fullard L, Lube G, Davies C, Dufek J (2019) The Permeability of Volcanic Mixtures - Implications for Pyroclastic Currents. Journal of Geophysical Research: Solid Earth 124:1343–1360. https://doi.org/1310.1029/2018JB016544

Buesch DC (1992) Incorporation and redistribution of locally derived lithic fragments within a pyroclastic flow. Geol Soc Am Bull 104:1193–1207. doi: 10.1130/0016-7606(1992)104<1193:IAROLD>2.3.CO;2

Bursik MI, Kurbatov A V., Sheridan MF, Woods AW (1998) Transport and deposition in the May 18, 1980, Mount St. Helens blast flow. Geology 26:155. doi: 10.1130/0091-7613(1998)026<0155:TADITM>2.3.CO;2

Bursik MI, Woods AW (1996) The dynamics and thermodynamics of large ash flows. Bull Volcanol 58:175–193. doi: 10.1007/s004450050134

Calabrò L., Esposti Ongaro T., Giordano G., de'Michieli Vitturi M. (2022). Reconstructing Pyroclastic Currents' Source and Flow Parameters from Deposit Characteristics and Numerical Modelling: The Pozzolane Rosse Ignimbrite case study (Colli Albani, Italy). Journal of Geophysical Research: Solid Earth, e2021JB023637.

Calder ES, Sparks RSJ, Gardeweg MC (2000) Erosion, transport and segregation of pumice and lithic clasts in pyroclastic flows inferred from ignimbrite at Lascar Volcano, Chile. J Volcanol Geotherm Res 104:201–235. doi: 10.1016/S0377-0273(00)00207-9

Capaccioni B., Sarocchi D. (1996). Computer-assisted image analysis on clast shape fabric from the Orvieto-Bagnoregio ignimbrite (Vulsini District, central Italy): implications on the emplacement mechanisms. Journal of Volcanology and Geothermal Research, 70(1-2), 75-90.

Carcano S, Esposti Ongaro T, Bonaventura L, Neri A (2014) Influence of grain-size distribution on the dynamics of underexpanded volcanic jets. J Volcanol Geotherm Res 285:60–80. doi: 10.1016/j.jvolgeores.2014.08.003

Carey S, Sigurdsson H, Gardner JE, Criswell W (1990) Variations in column height and magma discharge during the May 18, 1980 eruption of Mount St. Helens. J Volcanol Geotherm Res 43:99–112. doi: 10.1016/0377-0273(90)90047-J

Cerminara M, Esposti Ongaro T, Berselli LC (2016) ASHEE-1.0: a compressible, equilibrium–Eulerian model for volcanic ash plumes. Geosci Model Dev 9:697–730. doi: 10.5194/gmd-9-697-2016

Chédeville C, Roche O (2014) Autofluidization of pyroclastic flows propagating on rough substrates as shown by laboratory experiments. Journal of Geophysical Research : Solid Earth. 1764–1776. doi: 10.1002/2013JB010554

Chédeville C, Roche O (2015) Influence of slope angle on pore pressure generation and kinematics of pyroclastic flows : insights from laboratory experiments. Bull Volcanol 77:96. doi: 10.1007/s00445-015-0981-4

Christiansen R, Peterson D (1981) Chronology of the 1980 eruptive activity. In: Lipman P, Mullineaux D (eds) The 1980 eruptions of Mount St. Helens, Washington. U.S. Geological Survey Professional Paper 1250, pp 17–30

Clark JD, Pickering KT (1996), Submarine Channels: Processes and Architecture, vol. 231 pp., Vallis Press, London.

Cole PD, Calder ES, Druitt TH, et al (1998) Pyroclastic flows generated by gravitational instability of the 1996–97 Lava Dome of Soufriere Hills Volcano, Montserrat. Geophys Res Lett 25:3425–3428. doi: 10.1029/98GL01510

Crandell D (1989) Gigantic debris avalanche of Pleistocene age from ancestral Mount Shasta Volcano, California, and debris avalanche hazard zonation. US Geol Surv Bull 1861 1–32

Crandell DR, Miller CD, Glicken HX, et al (1984) Catastrophic debris avalanche from ancestral Mount Shasta volcano, California. Geology 12:143. doi: 10.1130/0091-7613(1984)12<143:CDAFAM>2.0.CO;2

Criswell CW (1987) Chronology and pyroclastic stratigraphy of the May 18, 1980, eruption of Mount St. Helens, Washington

Criswell CW (2021) A revised narrative of the May 18, 1980 Plinian eruption of Mount St. Helens: Changes in the conduit and magma supply. J Volcanol Geotherm Res 419:107388. doi: 10.1016/j.jvolgeores.2021.107388

Dartevelle S (2004) Numerical modeling of geophysical granular flows: 1. A comprehensive approach to granular rheologies and geophysical multiphase flows. Geochemistry, Geophys Geosystems 5:. doi: 10.1029/2003GC000636

Diller JS (1915) Guidebook of the Western United States: Part D. The Shasta Route and Coast Line, No. 614. US Government Printing Office

Douillet GA (2021). The supercritical question for pyroclastic dune bedforms: An overview. Sedimentology, 68(4), 1698-1727.

Druitt TH (1992) Emplacement of the May 18, 1980 lateral blast deposit ENE of Mount St. Helens, Washington. Bull Volcanol 54:554–572. doi: 10.1007/BF00569940

Dufek J (2016) The Fluid Mechanics of Pyroclastic Density Currents. Annu Rev Fluid Mech 48:459–485. doi: 10.1146/annurev-fluid-122414-034252

Eichelberger JC, Hayes DB (1982) Magmatic model for the Mount St. Helens blast of May 18, 1980. J Geophys Res 87:7727. doi: 10.1029/JB087iB09p07727

Elliott T (2000), Megaflute erosion surfaces and the initiation of turbidite channels, Geology, 28(2), 119–122.

Esposti Ongaro T, Cavazzoni C, Erbacci G et al. (2007) A parallel multiphase flow code for the 3D simulation of explosive volcanic eruptions. Parallel Comput 33:541–560. doi: 10.1016/j.parco.2007.04.003

Esposti Ongaro T, Cerminara M, Charbonnier SJ, et al (2020) A framework for validation and benchmarking of pyroclastic current models. Bull Volcanol 82:51. doi: 10.1007/s00445-020-01388-2

Esposti Ongaro T, Widiwijayanti C, Clarke AB, et al (2011) Multiphase-flow numerical modeling of the May 18, 1980 lateral blast at Mount St. Helens, USA. Geology 39:535–538. doi: 10.1130/G31865.1

Esposti Ongaro T, Clarke AB, Voight B, et al (2012) Multiphase flow dynamics of pyroclastic density currents during the May 18, 1980 lateral blast of Mount St. Helens. J Geophys Res Solid Earth 117:1–22. doi: 10.1029/2011JB009081

Esposti Ongaro T, Neri A, Menconi G et al. (2008) Transient 3D numerical simulations of column collapse and pyroclastic density current scenarios at Vesuvius. J Volcanol Geotherm Res 178:378–396. doi: 10.1016/j.jvolgeores.2008.06.036

Fan Y, Hill KM (2015) Shear-induced segregation of particles by material density. Phys Rev E 92:022211. doi: 10.1103/PhysRevE.92.022211

Farin M, Mangeney A, Roche O (2014) Fundamental changes of granular flow dynamics, deposition, and erosion processes at high slope angles: Insights from laboratory experiments. J Geophys Res Earth Surf 119:504–532. doi: 10.1002/2013JF002750

Fildani AS, Hubbard M, Covault JA, Maier KL, Romans BW, Traer M, Rowland JC (2013) Erosion at inception of deep-sea channels, Mar. Pet. Geol., 41, 48–61, doi:10.1016/j.marpetgeo.2012.03.006.

Fisher RV (1990) Transport and deposition of a pyroclastic surge across an area of high relief: The May 18, 1980 eruption of Mount St. Helens, Washington. Geol Soc Am Bull 102:1038–1054. doi: 10.1130/0016-7606(1990)102<1038:TADOAP>2.3.CO;2

Fisher RV, Glicken HX, Hoblitt RP (1987) May 18, 1980, Mount St. Helens deposits in South Coldwater Creek, Washington. J Geophys Res Solid Earth 92:10267–10283. doi: 10.1029/JB092iB10p10267

Forterre Y, Pouliquen O (2003) Long-surface-wave instability in dense granular flows. J Fluid Mech 486:S0022112003004555. doi: 10.1017/S0022112003004555

Fries A, Roche O, Carazzo G (2021) Granular mixture deflation and generation of pore fluid pressure at the impact zone of a pyroclastic fountain: Experimental insights. J Volcanol Geotherm Res 414:107226. https://doi.org/10.1016/j.jvolgeores.2021.107226.

Gardner JE, Nazworth C, Helper MA, Andrews BJ (2018) Inferring the nature of pyroclastic density currents from tree damage: The May 18, 1980 blast surge of Mount St. Helens, USA. Geology 46:795–798. doi: 10.1130/G45353.1

Gase AC, Brand BD, Bradford JH (2017) Evidence of erosional self-channelization of pyroclastic density currents revealed by ground-penetrating radar imaging at Mount St. Helens, Washington (USA). Geophys Res Lett 44:2220–2228. doi: 10.1002/2016GL072178

Giordano G, Cas RAF (2021) Classification of ignimbrites and their eruptions. Earth-Science Rev 220:103697. doi: 10.1016/j.earscirev.2021.103697

Giordano G, Zanella E, Trolese M, et al (2018) Thermal interactions of the AD79 Vesuvius pyroclastic density currents and their deposits at Villa dei Papiri (Herculaneum archaeological site, Italy). Earth Planet Sci Lett 490:180–192. doi: 10.1016/j.epsl.2018.03.023

Girolami L, Druitt TH, Roche O (2015) Towards a quantitative understanding of pyroclastic flows: Effects of expansion on the dynamics of laboratory fluidized granular flows. J Volcanol Geotherm Res 296:31–39. doi: 10.1016/j.jvolgeores.2015.03.008

Girolami L, Roche O, Druitt TH, Corpetti T (2010) Particle velocity fields and depositional processes in laboratory ash flows, with implications for the sedimentation of dense pyroclastic flows. Bull Volcanol 72:747–759. doi: 10.1007/s00445-010-0356-9

Glicken H (1996) Rockslide-debris avalanche of May 18, 1980, Mount St. Helens Volcano. Washington U S Geol Surv Open-file Rep 96-677

Gorshkov GS (1959) Gigantic eruption of the volcano bezymianny. Bull Volcanol 20:77–109. doi: 10.1007/BF02596572

Gorshkov GS (1963) Directed volcanic blasts. Bull Volcanol 26:83–88. doi: 10.1007/BF02597277

Harris DM, Rose WI, Roe R, Thompson MR (1981) Radar observations of ash eruptions. US Geol Surv Prof Pap 1250 323-334.

Hoblitt RP, Harmon RS (1993). Bimodal density distribution of cryptodome dacite from the 1980 eruption of Mount St. Helens, Washington. Bull Volcanol 55(6):421-437.

Hoblitt RP (2000) Was the May 18, 1980 lateral blast at Mt St. Helens the product of two explosions? Philos Trans R Soc London Ser A Math Phys Eng Sci 358:1639–1661. doi: 10.1098/rsta.2000.0608

Hoblitt RP (1986) Observations of the Eruptions of July 22 and August 7, 1980 at Mount St. Helens, Washington, No. 1335

Hoblitt RP, Miller CD, Vallance JW (1981) Origin and stratigraphy of the deposit produced by the May 18 directed blast. US Geol Surv Prof Pap 1250 401–419

Holosek, RE, Self, S, (1995) GOES weather satellite observations and measurements of the May 18, 1980 Mount St. Helens eruption, J Geophys Res, 11, B5, p 8469-8487.

Hughes SR, Druitt TH (1998). Particle fabric in a small, type-2 ignimbrite flow unit (Laacher See, Germany) and implications for emplacement dynamics. Bulletin of Volcanology, 60: 125–136.

Iverson RM, Reid ME, Logan M, et al (2011) Positive feedback and momentum growth during debris-flow entrainment of wet bed sediment. Nat Geosci 4:116–121. doi: 10.1038/ngeo1040

Jessop DE, Kelfoun K, Labazuy P, Mangeney A, Roche O, Tilliere J-L, Trouillete M, Thibault G (2012). LiDAR derived morphology of the 1993 Lascar pyroclastic flow deposits, and implication for flow dynamics and rheology. JVolcanol Geotherm Res 245-246:81-97, doi: 10.1016/j.jvolgeores.2012.06.030.

Johnson CG, Kokelaar BP, Iverson RM et al. (2012) Grain-size segregation and levée formation in geophysical mass flows. J Geophys Res Earth Surf 117. doi: 10.1029/2011JF002185

Kieffer SW (1981) Fluid dynamics of the May 18 blast at Mount St. Helens. US Geol Surv Prof Pap 1250 379–400

Kieffer SW, Sturtevant B (1988) Erosional furrows formed during the lateral blast at Mount St. Helens, May 18, 1980. J Geophys Res 93:14793. doi: 10.1029/JB093iB12p14793

Klug C, Cashman KV (1994). Vesiculation of May 18, 1980, Mount St. Helens magma. Geology 22(5):468-472.

Klug C, Cashman KV (1996). Permeability development in vesiculating magmas: implications for fragmentation. BullVolcanol 58(2):87-100.

Kokelaar BP, Graham RL, Gray JMNT, Vallance JW (2014) Fine-grained linings of levéed channels facilitate runout of granular flows. Earth Planet Sci Lett 385:172–180. doi: 10.1016/j.epsl.2013.10.043

Komorowski J-C et al. (2013) Paroxysmal dome explosion during the Merapi 2010 eruption: Processes and facies relationships of associated high-energy pyroclastic density currents, J Volcanol Geotherm Res, http://dx.doi.org/10.1016/j.jvolgeores.2013.01.007

Kuntz M, Rowley P, Macleod N (1990) Geologic map of pyroclastic flow and related deposits of the 1980 eruptions of Mount St. Helens, Washington: U.S. Geological Survey Miscellaneous Investigations Map I-1950, 1:12,000

Kuntz MA, Rowley PD, Macleod NS, et al (1981) Petrography and particle-size distribution of pyroclastic-flow, ash-cloud, and surge deposits. In: Lipman L, Mullineaux D (eds) The 1980 Eruptions of Mount St. Helens, Washington. U.S. Geological Survey Professional Paper 1250, pp. 525–540

Lesti C, Porreca M, Giordano G et al. (2011) High-temperature emplacement of the Cerro Galán and Toconquis Group ignimbrites (Puna plateau, NW Argentina) determined by TRM analyses. Bull Volcanol 73:1535–1565. doi: 10.1007/s00445-011-0536-2

Lipman P, Moore J, Swanson D (1981) Bulging of the north flank before the May 18 eruption. US Geol Surv Prof Pap 1250 143–156

Lube G, Breard ECP, Esposti-Ongaro T, et al (2020) Multiphase flow behaviour and hazard prediction of pyroclastic density currents. Nat Rev Earth Environ 1:348–365. doi: 10.1038/s43017-020-0064-8

Mack S (1960) Geology and ground-water features of Shasta Valley, Siskiyou County, California. US Government Printing Office

Mackaman-Lofland C, Brand BD, Taddeucci J, Wohletz K (2014) Sequential fragmentation/transport theory, pyroclast size–density relationships, and the emplacement dynamics of pyroclastic density currents — A case study on the Mt. St. Helens (USA) 1980 eruption. J Volcanol Geotherm Res 275:1–13. doi: 10.1016/j.jvolgeores.2014.01.016

Major JJ (2000) Gravity-driven consolidation of granular slurries - implications for debris-flow deposition and deposit characteristics. J SedimRes 70(1):64-83

Mangeney A, Roche O, Hungr O, et al (2010) Erosion and mobility in granular collapse over sloping beds. J Geophys Res Earth Surf 115:. doi: 10.1029/2009JF001462

Moore J, Albee W, Lipman P, Mullineaux D (1981) Topographic and structural changes, March–July 1980: photogrammetric data. US Geol Surv Prof Pap 1250 123–134

Moore J, Rice C (1984) Chronology and character of the May 18, 1980, explosive eruption of Mount St. Helens. In: Explosive volcanism: Inception, evolution, hazards. National Academy Press, Washington, D.C., pp 133–142

Moore J, Sisson TW (1981) Deposits and effects of the May 18 pyroclastic surge. US Geol Surv Prof Pap 1250 421–438

Mullineaux D, Crandell D (1981) The eruptive chronology of Mount St. Helens. US Geol Surv Prof Pap 1250 3–15

Neri A, Esposti Ongaro T, Macedonio G, Gidaspow D (2003) Multiparticle simulation of collapsing volcanic columns and pyroclastic flow. J Geophys Res Solid Earth 108:. doi: 10.1029/2001JB000508

Orescanin MM, Austin JM, Kieffer SW (2010) Unsteady high-pressure flow experiments with applications to explosive volcanic eruptions. J Geophys Res 115:B06206. doi: 10.1029/2009JB006985

Palladino DM (2017) Simply pyroclastic currents. Bull Volcanol 79:53. doi: 10.1007/s00445-017-1139-3

Pallister JS, Clynne MA, Wright HM, et al (2017) Field-trip guide to Mount St. Helens, Washington—An overview of the eruptive history and petrology, tephra deposits, 1980 pyroclastic density current deposits, and the crater. US Geol Surv Sci Investig Rep 2017-5022-D 65 p. doi: 10.3133/sir20175022D

Paterson GA, Roberts AP, Mac Niocaill C, et al (2010) Paleomagnetic determination of emplacement temperatures of pyroclastic deposits: an under-utilized tool. Bull Volcanol 72:309–330. doi: 10.1007/s00445-009-0324-4

Pensa A, Capra L, Giordano G (2019) Ash clouds temperature estimation. Implication on dilute and concentrated PDCs coupling and topography confinement. Sci Rep 9:5657. doi: 10.1038/s41598-019-42035-x

Pollock NM, Brand BD, Roche O (2016) The controls and consequences of substrate entrainment by pyroclastic density currents at Mount St. Helens, Washington (USA). J Volcanol Geotherm Res 325:135–147. doi: 10.1016/j.jvolgeores.2016.06.012

Pollock NM (2019) Synthesizing Field and Experimental Techniques to Investigate the Enigmatic Processes Occurring at the Base of Pyroclastic Currents. Boise State University Theses and Dissertations. 1599. doi: 10.18122/td/1599/boisestate

Pollock NM, Brand BD, Rowley PJ et al. (2019) Inferring pyroclastic density current flow conditions using syn-depositional sedimentary structures. Bull Volcanol 81:46. doi: 10.1007/s00445-019-1303-z

Porreca M, Mattei M, MacNiocaill C, et al (2008) Paleomagnetic evidence for low-temperature emplacement of the phreatomagmatic Peperino Albano ignimbrite (Colli Albani volcano, Central Italy). Bull Volcanol 70:877–893. doi: 10.1007/s00445-007-0176-8

Pouliquen O, Delour J, Savage SB (1997) Fingering in granular flows. Nature 386:816-817

Pouliquen O, Vallance JW (1999) Segregation induced instabilities of granular fronts. Chaos An Interdiscip J Nonlinear Sci 9:621–630. doi: 10.1063/1.166435

Roche O (2012), Depositional processes and gas pore pressure in pyroclastic flows: An experimental perspective, Bull. Volcanol 74(8):1807–1820, doi:10.1007/s00445-012-0639-4.

Roche O (2015) Nature and velocity of pyroclastic density currents inferred from models of entrainment of substrate lithic clasts. Earth Planet Sci Lett 418:115–125. doi: 10.1016/j.epsl.2015.03.001

Roche O, Niño Y, Mangeney A, et al (2013) Dynamic pore-pressure variations induce substrate erosion by pyroclastic flows. Geology 41:1107–1110. doi: 10.1130/G34668.1

Roche O, Azzaoui N., Guillin A (2021). Discharge rate of explosive volcanic eruption controls runout distance of pyroclastic density currents. Earth Planet SciLett, 568:117017.

Rowley P, Kuntz M, Macleod N (1981) Pyroclastic-Flow Deposits. In: Lipman P, Mullineaux D (eds). U.S. Geological Survey Professional Paper 1250, pp 489–512

Rowley PJ, Kokelaar P, Menzies M, Waltham D (2011) Shear-Derived Mixing In Dense Granular Flows. J Sediment Res 81:874–884. doi: 10.2110/jsr.2011.72

Rowley PJ, Roche O, Druitt TH, Cas R (2014) Experimental study of dense pyroclastic density currents using sustained, gas-fluidized granular flows. Bull Volcanol 76:1–13. doi: 10.1007/s00445-014-0855-1

Sisson TW (1995) Blast ashfall deposit of May 18, 1980 at Mount St. Helens, Washington. J Volcanol Geotherm Res 66:203–216. doi: 10.1016/0377-0273(94)00063-M

Shimizu, H. A., Koyaguchi, T., & Suzuki, Y. J. (2019). The run-out distance of large-scale pyroclastic density currents: a two-layer depth-averaged model. JVolcanolGeotherm Res, 381:168-184.

Sousa J, Voight B (1995) Multiple-pulsed debris avalanche emplacement at Mount St. Helens in 1980: Evidence from numerical continuum flow simulations. J Volcanol Geotherm Res 66:227–250. doi: 10.1016/0377-0273(94)00067-Q

Smith G, Rowley P, Williams R, Giordano G, Trolese M, Silleni A, Parsons DR,Capon S (2020) A bedform phase diagram for dense granular currents. Nat.omm., 11(1):1-11.

Sparks RSJ, Moore JG, Rice CJ (1986) The initial giant umbrella cloud of the May 18, 1980 explosive eruption of Mount St Helens, J Geophys Res 28, p 257-274.

Sparks RSJ, Gardeweg MC, Calder ES, Matthews SJ (1997) Erosion by pyroclastic flows on Lascar Volcano, Chile. Bull Volcanol 58:557–565. doi: 10.1007/s004450050162

Sparks RSJ, Barclay J, Calder ES, Herd RA, Komorowski JC, Luckett R, Norton GE, Ritchie LJ, Voight B,Woods AW (2002) Generation of a debris avalanche and violent pyroclastic density current on 26 December (Boxing Day) 1997 at Soufriere Hills Volcano, Montserrat. *Geological Society, London, Memoirs*, *21*(1):409-434.

Sulpizio R, Dellino P, Doronzo DM, Sarocchi D. (2014) Pyroclastic density currents: state of the art and perspectives. J Volcanol Geotherm Res *283*:36-65.

Taylor GA (1958) The 1951 eruption of Mount Lamington, Papua. Aust. Bur. Miner. Resour. Geol. Geophys. Bull. *38*:1-117.

Trolese (2022). Data repository, https://doi.org/10.5281/zenodo.7191383.

Trolese M, Cerminara M, Esposti Ongaro T, Giordano G (2019) The footprint of column collapse regimes on pyroclastic flow temperatures and plume heights. Nat Commun 10:2476. doi: 10.1038/s41467-019-10337-3

Trolese M, Giordano G, Cifelli F et al. (2017) Forced transport of thermal energy in magmatic and phreatomagmatic large volume ignimbrites: Paleomagnetic evidence from the Colli Albani volcano, Italy. Earth Planet Sci Lett 478:179–191. doi: 10.1016/j.epsl.2017.09.004

Trolese M, Giordano G, Komorowski J-C et al. (2018) Very rapid cooling of the energetic pyroclastic density currents associated with the 5 November 2010 Merapi eruption (Indonesia). J Volcanol Geotherm Res 358:1–12. doi: 10.1016/j.jvolgeores.2018.06.004

Valderrama P, Roche O, Samaniego P, Van Wyk de Vries B, Araujo G (2018) Granular fingering as a mechanism for ridge formation in debris avalanche deposits: Laboratory experiments and implications for Tutupaca volcano, Peru. J VolcanolGeotherm Res 349:409-418, doi: https://doi.org/410.1016/j.jvolgeores.2017.1012.1004

Valentine GA, Sweeney MR (2018) Compressible Flow Phenomena at Inception of Lateral Density Currents Fed by Collapsing Gas-Particle Mixtures. J Geophys Res Solid Earth 123:1286–1302. doi: 10.1002/2017JB015129

Valentini L, Capaccioni B, Rossi PL, Scandone R, Sarocchi D (2008) Vent area and depositional mechanisms of the Upper Member of the Neapolitan Yellow Tuff (Campi Flegrei, Italy): new insights from directional fabric through image analysis. Bulletin of Volcanol70(9):1087-1101.

Vallance JW, Kokelaar PB., Van Eaton AR (2017) Day 1: 1980 pyroclastic-flow deposits: in Pallister, J.S., Clynne, M.A., Wright, H.M., Van Eaton, A.R., Vallance, J.W., Sherrod, D.R., and Kokelaar, B.P., 2017, Field-trip guide to Mount St. Helens, Washington—An overview of the eruptive history and petrology, tephra deposits, 1980 pyroclastic density current deposits, and the crater. US Geol Sur Sci Investig Rep 2017–5022–D, p. 25–42. doi: 10.3133/sir20175022D

Voight B (1981) Time scale for the first moments of the May 18 eruption. US Geol Surv Prof Pap 1250 69–86

Voight B, Glicken H, Janda R, Douglass P (1981) Catastrophic rockslide-avalanche of May 18. US Geol Surv Prof Pap 1250 347–378

Voight B, Janda RJ, Glicken H, Douglass PM (1983) Nature and mechanics of the Mount St. Helens rockslide-avalanche of May 18, 1980. Géotechnique 33:243–273. doi: 10.1680/geot.1983.33.3.243

Voight B, Komorowski JC, Norton GE, Belousov AB, Belousova M, Boudon, G, Francis, P.W., Franz, W., Heinrich, P., Sparks, R.S.J. and Young, S.R., (2002). The 26 December (Boxing Day) 1997 sector collapse and debris avalanche at Soufriere Hills volcano, Montserrat. Geological Society, London, Memoirs, 21(1):363-407.

Waitt R (2015) In the path of destruction - eyewitness chronicles of Mount St. Helens. Washington State University Press

Waitt RB (1981) Devastating pyroclastic density flow and attendant air fall of May 18 - Stratigraphy and sedimentology of deposits. US Geol Surv Prof Pap 1250 439–458

Walker GPL, McBroome LA (1983) Mount St. Helens 1980 and Mount Pelee 1902—Flow or surge? Geology 11:571. doi: 10.1130/0091-7613(1983)11<571:MSHAMP>2.0.CO;2

Williams H (1932) Mount Shasta, a Cascade volcano. J Geol 40:417–429

Wilson L, Head J (1981) Morphology and rheology of pyroclastic (of Mount St. Helens) flows and their deposits and guidelines for future observations. US Geol Surv Prof Pap 1250 513–524

Wohletz KH, Sheridan MF, Brown WK (1989) Particle size distributions and the sequential fragmentation/transport theory applied to volcanic ash. J Geophys Res Solid Earth 94:15703–15721. doi: 10.1029/JB094iB11p15703

Xiao H, Umbanhowar PB, Ottino JM, Lueptow RM (2016) Modelling density segregation in flowing bidisperse granular materials. Proc R Soc A Math Phys Eng Sci 472:20150856. doi: 10.1098/rspa.2015.0856

Zrelak PJ, Pollock NM, Brand BD, et al (2020) Decoding pyroclastic density current flow direction and shear conditions in the flow boundary zone via particle-fabric analysis. J Volcanol Geotherm Res 402:106978. doi: 10.1016/j.jvolgeores.2020.106978

Table Captions:

Table 1. 1980 Explosive eruptions of Mount St. Helens after May 18.

Table 2: Unit thickness with distance from source. Distances are approximated from the center of the crater. Text in gray indicates not fully exposed (base buried or top eroded), italicized text is estimated and "—" indicates unexposed. See Brand et al., (2014) for full dataset.

Table 3: Geometric data for four main flow units from the afternoon boil-over PC activity on 18 May 1980. Equivalent runout distance is the radius of a circle of equivalent area. Equivalent diameter is the diameter of the circle with an area equivalent to that of the ignimbrite areal extent. The aspect ratio is the average thickness divided by the equivalent diameter. Mass discharge from Carey et al., 1990.

Figure Captions:

Figure 1: Map showing the distribution of the May 18, 1980 blast-PC and afternoon PC deposits. The proximal, medial and distal delineations are from Fisher (1990).

Figure 2: Pyroclastic currents generated during the 18 May 1980 eruption and their associated phases (see Figure 3 for phases). Photographs (a – d), provided by photographer K. Seibert (Vancouver, WA). These photos were taken from ~33 km south-southeast of MSH. For scale, the elevation of the new crater rim is 2549 m and has a local relief of ~1200 m. Photographs (e, f) come from the J. Rosenbaum sequence and (g, h) from the R. Christiansen sequence; they are available through the USGS library.

Figure 3: Summary of phases during the May 18, 1980, eruption at MSH (modified from Pallister et al., 2018). Times shown in Pacific Daylight Time (PDT). Eruptive phases I-VI are adopted from Criswell (1987). Plume heights represent maximum heights from GOES satellite (Sparks et al., 1986; Holasek and Self, 1995) and radar (Harris et al., 1981). "PCs" and greyscale bars at bottom indicate onset and duration of different PC emplacement periods. lpf, mpf, and upf refer to the stratigraphic position of the PC deposits; lower, middle, and upper, respectively, from Criswell (1987). Flow Unit designation from Brand et al. (2014). a.s.l. is above sea level. The star represents the coinciding M 5.2 earthquake and onset of the eruption. Mass flux estimates are from Carey et al. (1990).

Figure 4: MSH Blast stratigraphy; stratigraphic labeling of Belousov et al. (2007). Layer A = poorly sorted mixture of substrate material and pumice. Layer B = Massive, clast supported, and fines depleted layer with charred vegetation and wood fragments. Layer C = fines-enriched, matrix-supported, poorly sorted massive deposit. Layer D = thin fines rich and accretionary lapilli-bearing deposit. Photo courtesy of Sasha Belousov.

Figure 5: Volumetric particle concentration of pyroclasts (logarithmic scale) on a vertical slice along the north section of Mount St. Helens, as resulting from the numerical simulation of the 1980 blast event (modified after Esposti Ongaro et al., 2011). Numerical results are overlaid on an oblique view of the blast deposit (subdivided into the three main regions described by Hoblitt et al., 1981).

Figure 6: Map of the Pumice Plain showing debris avalanche and afternoon PC deposit distribution. Red arrows indicate flow lines, summarized from Zrelak et al., 2020. Green-black dots are outcrop locations referenced in the other figures. Black box indicates where flows traveling down the northwest flank and stairstep region converged. Brackets indicate average slope angles.

Figure 7: (a)–(d) Granulometry data comparing Pumice Plain units to proximal bedded deposits (PBD) and inner crater deposits. Md φ: median grain size,σ: grain size sorting, F2/F1:ratio of F2 ash (<62.5 μm) to F1 ash (<1 mm). Solid lines in (d) represent the Walker (1984) pyroclastic flow (concentrated PC) field, whereas the dotted lines represent their pyroclastic surge (dilute PC) field.

Figure 8: Deposits of flow units I-IV, modified from Brand et al., (2014). The location, named AD-1, is noted on the map in Figure 6.

Figure 9: Flank deposits to eastern Pumice Plain. Flow direction is right to left for all panels, including the experiment snapshot in (c). Photos (a) and (b) show regressive bedforms with a series of steeply-dipping backset beds. (c) Photo from the experiments of Smith et al (2020) showing the development of a 'granular bore' and similar deposit features to (b). (d) and (e) Photograph and sketch of the transitional deposits found midflank. Photos in a and b are noted as PBD_1 for proximal deposit; photo in d is noted as PBD_2 for the transitional deposits (see locations in Figure 6).

Figure 10: Examples of recumbent flame structures both within the May 18, 1980 PC deposits (a-c) and experimentally-produced structures (d-f; from Pollock 2019). Flow direction is left to right in all photographs. Yellow lines added to emphasize structures in (b) and (c). The locations of the structures found at MSH, named B-3 (a), C-4 (b), and AD-3 (c), respectively, are noted on the map in Figure 6. Note the increase in length of the experimentally-produced structures from 0.5–1.5 cm in panel 10d to 8–10 cm in panel 10f corresponding to increases in flow front velocity. Red line indicates flow top.

Figure 11: (a) and (b) show large scour and fill feature in the northwest Pumice Plain, associated with Units III and IV (modified from Brand et al., 2014). The lower block lens within the scour (Unit III) contains vent-derived lithic clasts. The upper lithic lens was inaccessible for sampling. On left side of outcrop, pumice lens (plens) and strata dip away from the channel axis suggesting an outer-channel facies. Photo (c) shows a lithic-rich wedge of PC deposits nestled within a paleo-valley within the debris avalanche deposit (Location B-2 in Figure 6). The transparent white line denotes the contact between the debris avalanche hummock and the wedge of PDC deposits. The layer of lithic clasts just above the debris avalanche contact was determined to be eroded from hummocks upslope (Brand et al., 2017).

Figure 12. Photograph looking eastward of Mount St. Helens erupting on July 22, 1980 at 1901 PDT. The photo is taken at the beginning of the third eruptive pulse. A pyroclastic current moving rapidly northward from the crater is visible. U.S. Geological Survey photograph taken by J. Vallance.

Figure 13. Photograph showing PC deposit of July 22, 1980 at Mount St. Helens. The photograph illustrates early stage spreading, multiple nested levee pairs, and complex sequence of late-stage, overlapping lobes. U.S. Geological Survey photograph taken by N. Macleod.

Figure 14. A. Schematic cutaway illustration of the process leading to formation of lateral levées behind a debris-flow front. Red path shows how coarse grain near surface migrates toward a levée. Reference frame moves at speed of advancing flow so that a grain advancing less rapidly than flow front appears to move backwards (see Johnson et al., 2012). We infer that coarse particles in a granular pyroclastic current with high solids fraction circulate in a fashion similar to that in a debris flow to form levées and lobate termini. B. Lobe of July 1980 pumiceous PC deposit on the Pumice Plain at Mount St. Helens (photographed in 2010). The flow-head deposit shows characteristic bulbous form, about 1 m thick (pole is 1 m), while the levées behind maintain the same form and grain-size characteristics as they bound channel-flow deposit for >250 m into the distance. We note that post depositional consolidation was variable with initially inflated channel deposits experiencing more deflation after deposition than levées. Sparse meter-scale blocks between the levées (middle distance) are a stranded 'bed-load' of relatively dense rock presumed to have rolled

or slid along the channel driven and to have been partially supported by the channel-flow mixture. The substrate slope is approximately 4°. Adapted from Pallister et al. (2017).

Figure 15: Collection of emplacement temperature data from the 1980 MSH eruptions.

Supplementary Figure Captions:

Supplementary Figure 1: Isopach map of Unit 1. Lines outlined in black delimit topographic highs where no PC deposits exist (i.e. thickness of deposits inside these emboldened lines is zero).

Supplementary Figure 2: Isopach map of Unit 2. Lines outlined in black delimit topographic highs where no PC deposits exist (i.e. thickness of deposits inside these emboldened lines is zero).

Supplementary Figure 3: Isopach map of Unit 3. Lines outlined in black delimit topographic highs where no PC deposits exist (i.e. thickness of deposits inside these emboldened lines is zero).

Supplementary Figure 4: Isopach map of Unit 4. Lines outlined in black delimit topographic highs where no PC deposits exist (i.e. thickness of deposits inside these emboldened lines is zero).

Supplementary Figure 5: PC volume for each unit is the integration of the area under each curve.

Table 1. 1980 Explosive eruptions of Mount St. Helens after May 18.

Date	Time	Flow unit	Duration	Plume height (km)	Runout (km)	Bulk Volume (km^3)	Area (km^2)
May 25	02:32	Pyroclastic flow (buried by June 12)		14	4 km	0.001	1.7
June 12	19:05 21:11 ?	No flow Pyroclastic flow(s) Dome	 Minutes?	11 15	--- 7.5	--- 0.01	--- 8.3
July 22	17:14 18:25 19:01	No flow Pyroclastic flow Pyroclastic flow total	- 5–10 min 5–10 min	14 18 14	--- 6.5 7.0	 0.006	 4.8
August 7	16:23 ?	Pyroclastic flow Dome	6.5 min	13	5.5	0.004	3.6
October 16 **October 17** **October 18**	21:58 09:28 21:12 12:35 14:32	? pyroclastic flow pyroclastic flow pyroclastic flow dome		13 14 14 8 6	? 4 4 small	 0.001	 2.3

Table 2: Unit thickness with distance from source. Distances are approximated from the center of the crater. Text in gray indicates not fully exposed (base buried or top eroded), italicized text is estimated and "—" indicates unexposed. See Brand et al., (2014) for full dataset.

Distance (km)	UTM	UTM	Unit I (m)	Unit II (m)	Unit III (m)	Unit IV (m)
4.8	562715.5	5121085	--	--	--	**7.8**
5.2	562525.2	5121364	--	--	**8**	**6**
5.6	561987	5121706	--	**3**	***9***	**10**
5.37	561906.6	5121691	**3**	**3.5**	**7**	**5**
5.6	561209.2	5121813	**2**	**7.5**	**6**	**5.3**
5.8	561238.8	5122078	**5.8**	**5.7**	**9.5**	**3**
5.8	562673	5122035	--	--	**4.5**	**5.6**
6.4	562299	5122507	--	--	--	**6**
7.1	561007	5122249	**10**	**8**	**5**	**2.8**
7.1	562314.6	5123490	**7**	**3.8**	**5**	**5.5**
7.2	562014.6	5123171	**10**	**4**	**3.9**	**7.7**
7.2	560984.9	5122402	**12**	**8**	**8**	**3**
7.2	560999.8	5122477	--	**4.33**	**8**	**3**
7.8	560833.1	5123276	**8.9**	**4**	**3.5**	**2.5**
8.4	560922	5123421	--	--	**4.5**	**5.7**

Table 3: Geometric data for four main flow units from the afternoon boil-over PC activity on May 18, 1980. Equivalent runout distance is the radius of a circle of equivalent area. Equivalent diameter is the diameter of the circle with an area equivalent to that of the ignimbrite areal extent. The aspect ratio is the average thickness divided by the equivalent diameter. Mass discharge from Carey et al., 1990.

Flow Unit	Runout Distance (km)	Average Thickness (m)	Area Covered (m^2)	Volume (km^3)	Equivalent runout (m)	Equivalent diameter (m)	Aspect Ratio	Mass discharge ($kg\ s^{-1}$)
Unit I	7.8	4.4	7.9×10^{6}	0.04	1586	3172	1.4×10^{-3}	6.3×10^{6}-1.3×10^{7}
Unit II	7.8	3.3	8.4×10^{6}	0.03	1635	3271	1.0×10^{-3}	6.3×10^{6}-1.3×10^{7}
Unit III	8.4	3.6	1.3×10^{7}	0.05	2003	4006	0.9×10^{-3}	3.9×10^{6}
Unit IV	8.4	4.7	1.2×10^{7}	0.06	1930	3860	1.2×10^{-3}	4.0×10^{7}

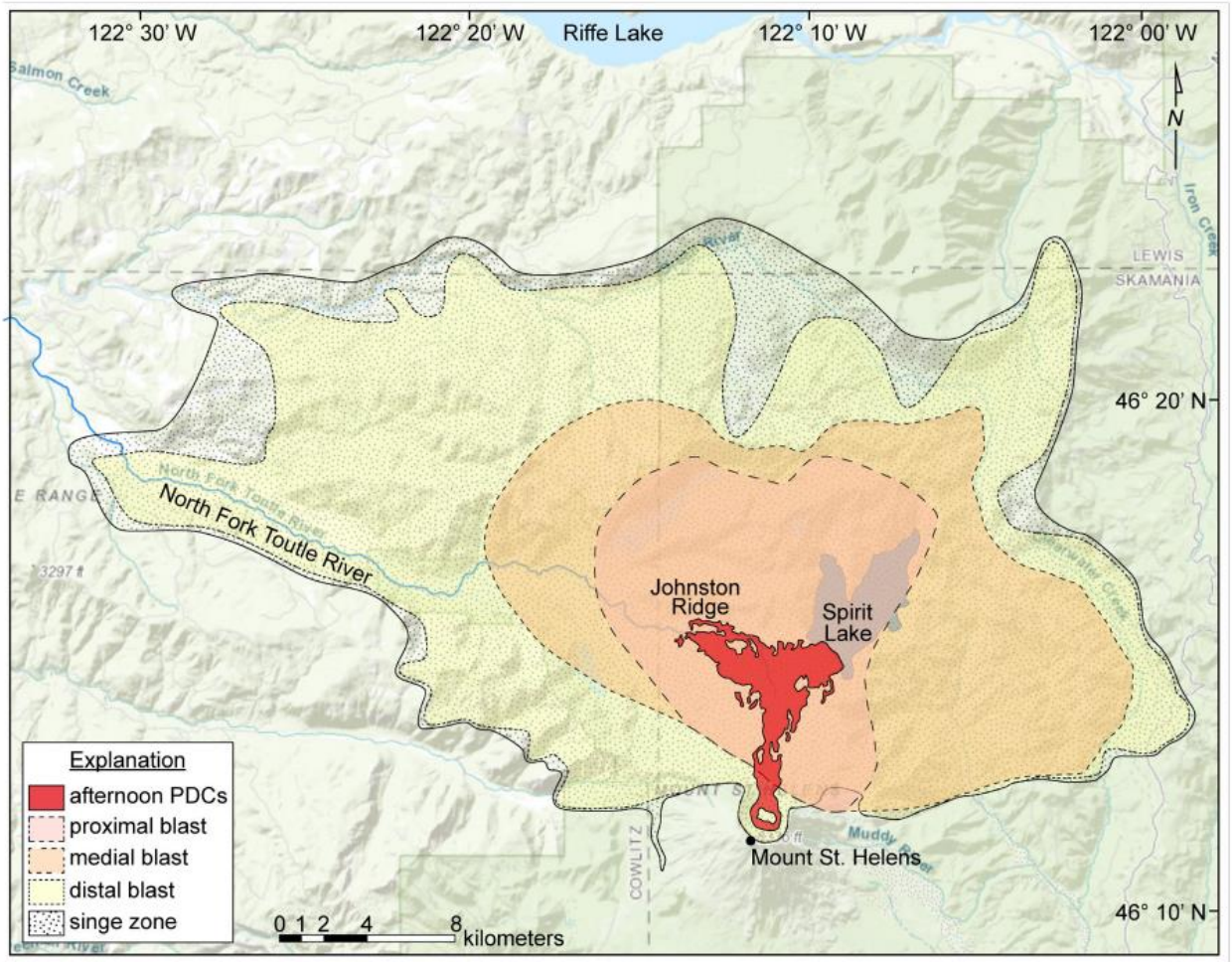

Figure 1: Map showing the distribution of the May 18, 1980 blast-PC and afternoon PC deposits. The proximal, medial and distal delineations are from Fisher (1990).

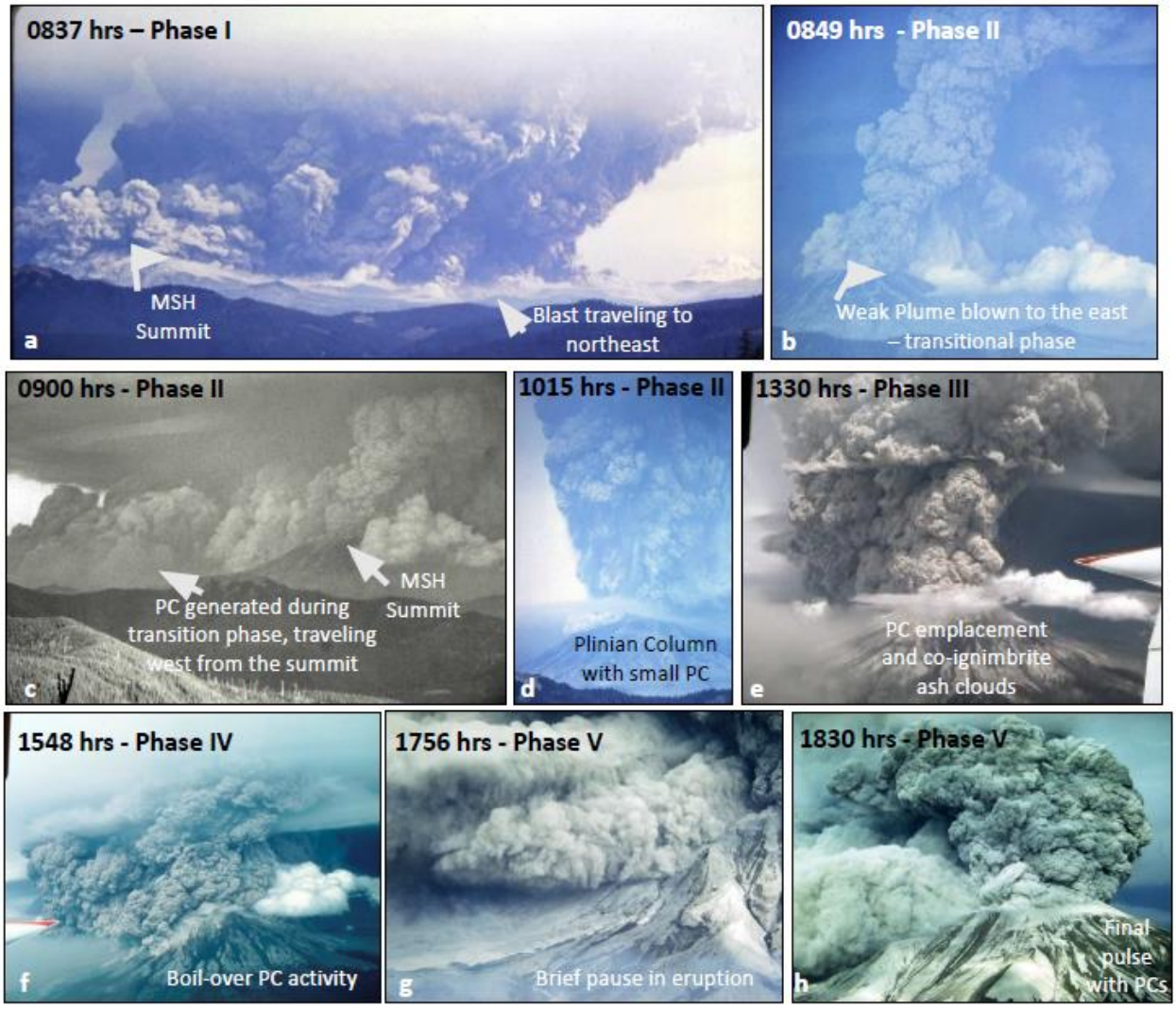

Figure 2: Pyroclastic currents generated during the 18 May 1980 eruption and their associated phases (see Figure 3 for phases). Photographs (a – d), provided by photographer K. Seibert (Vancouver, WA). These photos were taken from ~33 km south-southeast of MSH. For scale, the elevation of the new crater rim is 2549 m and has a local relief of ~1200 m. Photographs (e, f) come from the J. Rosenbaum sequence and (g, h) from the R. Christiansen sequence; they are available through the USGS library.

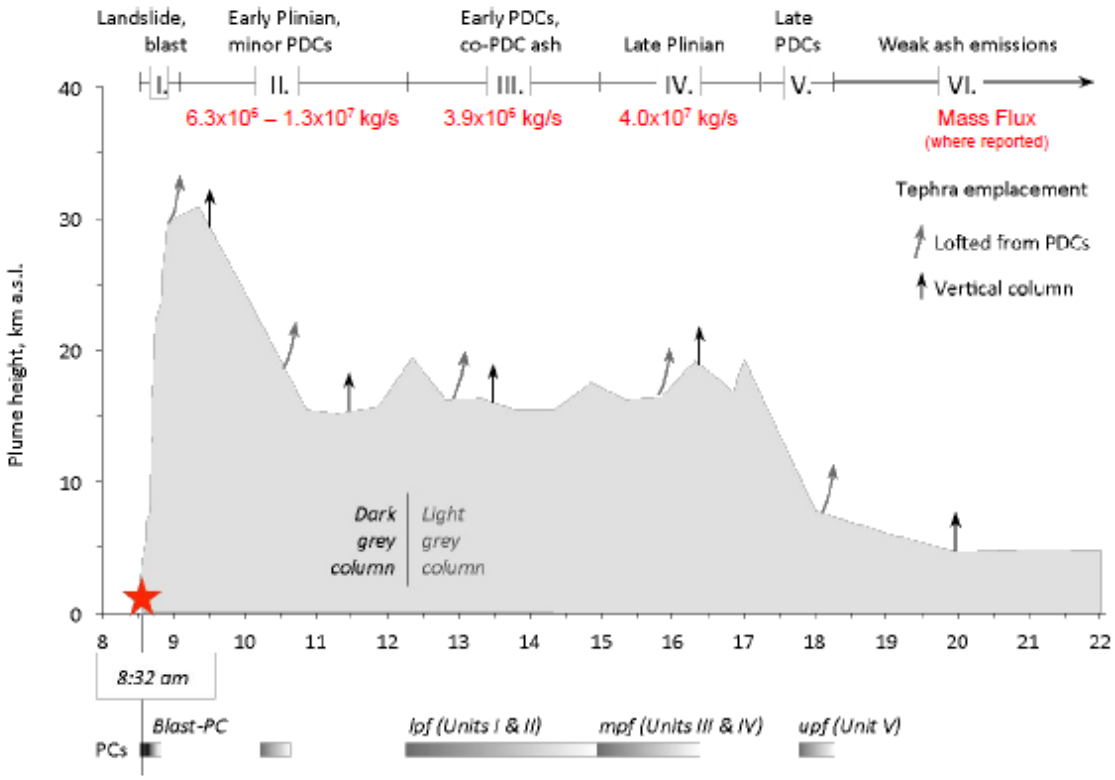

Figure 3: Summary of phases during the May 18, 1980, eruption at MSH (modified from Pallister et al., 2018). Times shown in Pacific Daylight Time (PDT). Eruptive phases I-VI are adopted from Criswell (1987). Plume heights represent maximum heights from GOES satellite (Sparks and otherset al., 1986; Holasek and Self, 1995) and radar (Harris et al., 1981). "PCs" and greyscale bars at bottom indicate onset and duration of different PC emplacement periods. lpf, mpf, and upf refer to the stratigraphic position of the PC deposits; lower, middle, and upper, respectively, from Criswell (1987). Flow Unit designation from Brand et al. (2014). a.s.l. is above sea level. The star represents the coinciding M 5.2 earthquake and onset of the eruption. Mass flux estimates are from Carey et al. (1990).

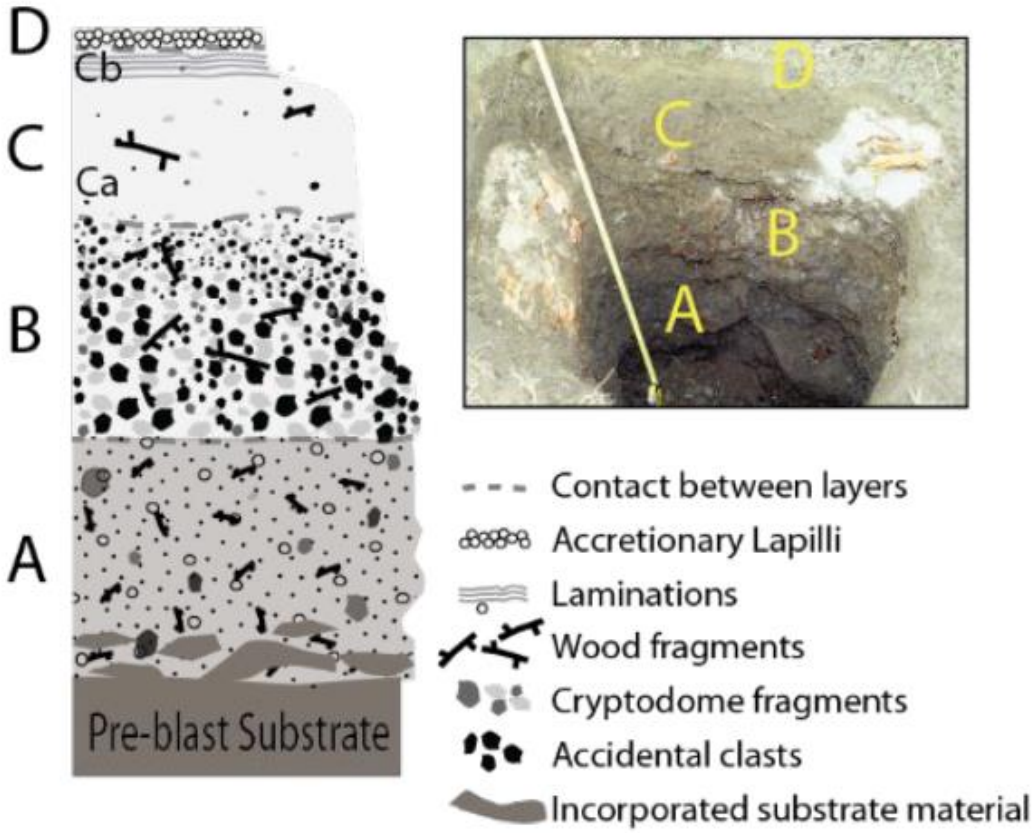

Figure 4: MSH Blast stratigraphy; stratigraphic labeling of Belousov et al. (2007). Layer A = poorly sorted mixture of substrate material and pumice. Layer B = Massive, clast supported, and fines depleted layer with charred vegetation and wood fragments. Layer C = fines-enriched, matrix-supported, poorly sorted massive deposit. Layer D = thin fines rich and accretionary lapilli-bearing deposit. Photo courtesy of Sasha Belousov.

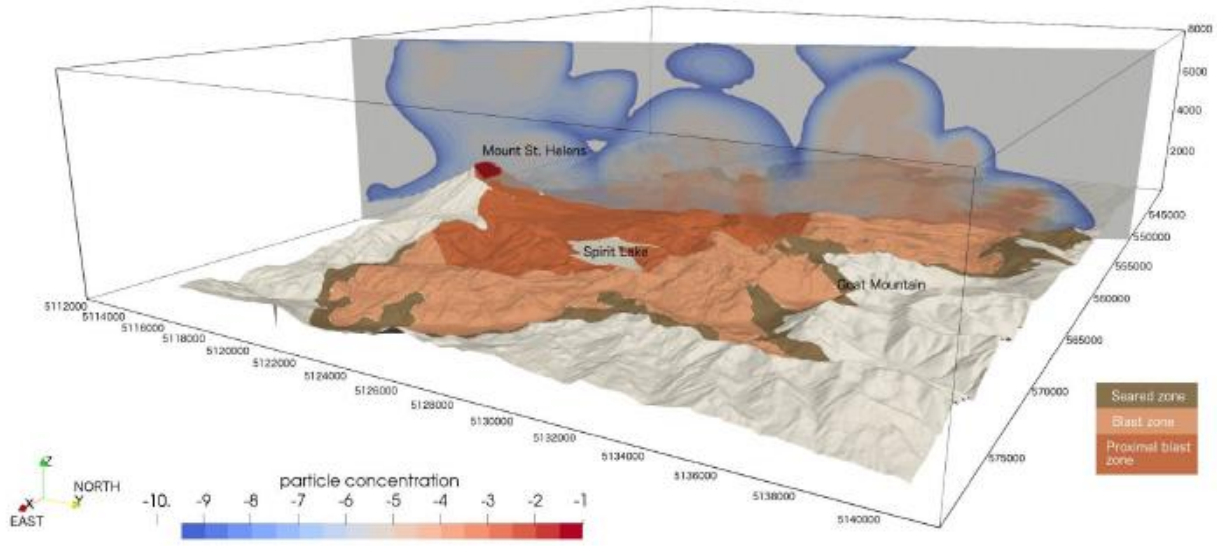

Figure 5: Volumetric particle concentration of pyroclasts (logarithmic scale) on a vertical slice along the north section of Mount St. Helens, as resulting from the numerical simulation of the 1980 blast event (modified after Esposti Ongaro et al., 2011). Numerical results are overlaid on an oblique view of the blast deposit (subdivided into the three main regions described by Hoblitt et al., 1981).

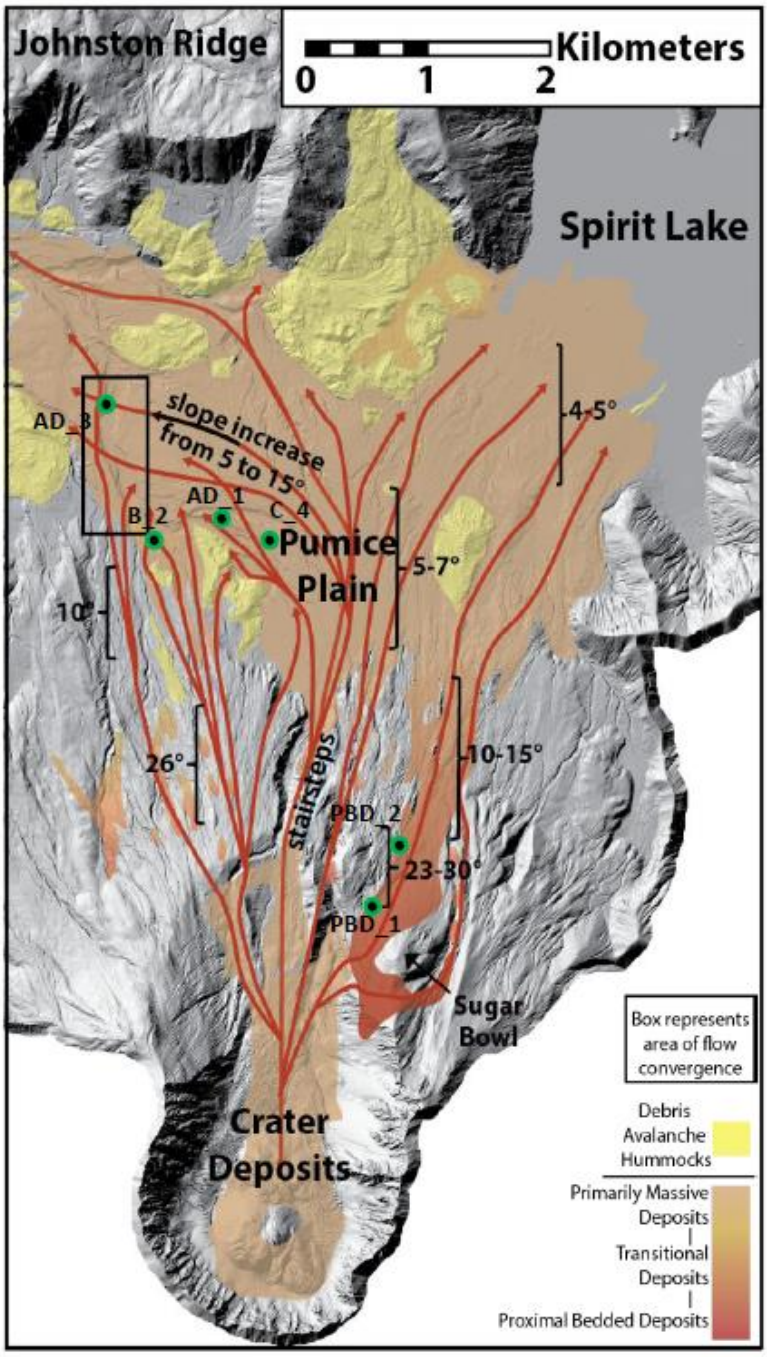

Figure 6: Map of the Pumice Plain showing debris avalanche and afternoon PC deposit distribution. Red arrows indicate flow lines, summarized from Zrelak et al., 2020. Green-black dots are outcrop locations referenced in the other figures. Black box indicates where flows traveling down the northwest flank and stairstep region converged. Brackets indicate average slope angles.

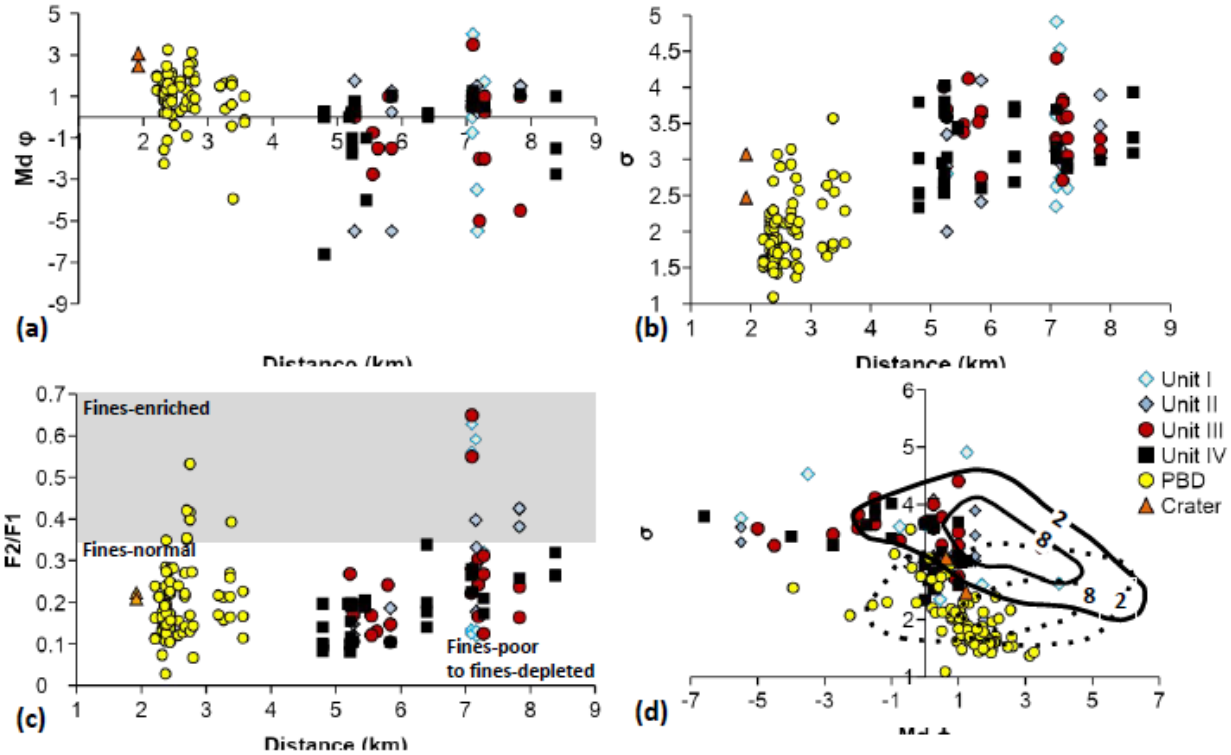

Figure 7: (a)–(d) Granulometry data comparing Pumice Plain units to proximal bedded deposits (PBD) bed and inner crater deposits:. Md φ: medianmean grain size,σ s: grain size sorting, F2/F1: ratio of F2 ash (<62.5 μm) to F1 ash (<1 mm). Solid lines in (d) represent the Walker (1984) pyroclastic flow (concentrated PC) field, whereas the dotted lines represent their pyroclastic surge (dilute PC) field.

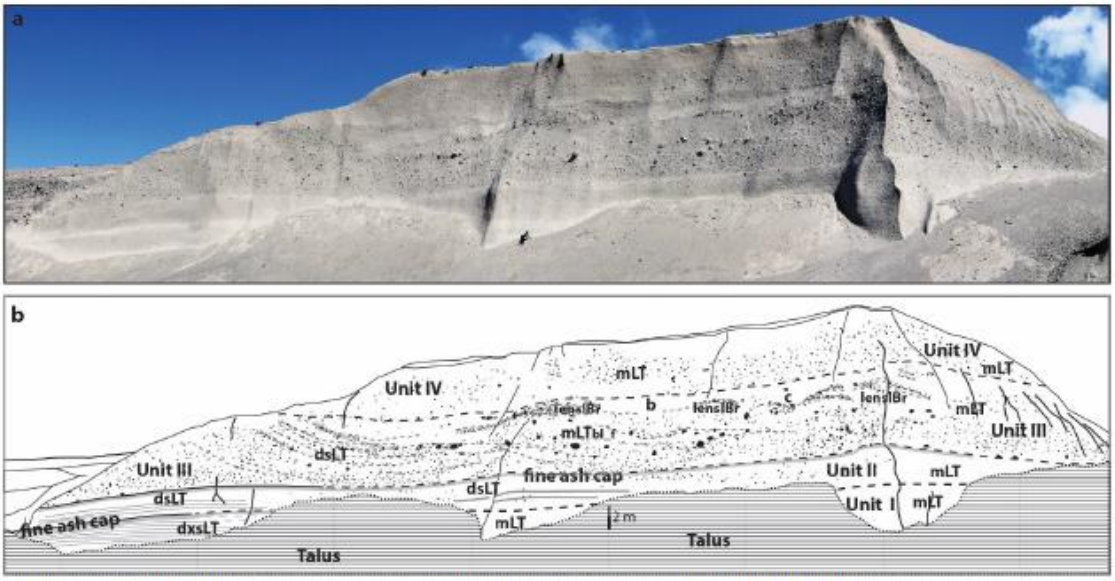

Figure 8: Deposits of flow units I-IV, modified from Brand et al., (2014). The location, named AD-1, is noted on the map in Figure 6.

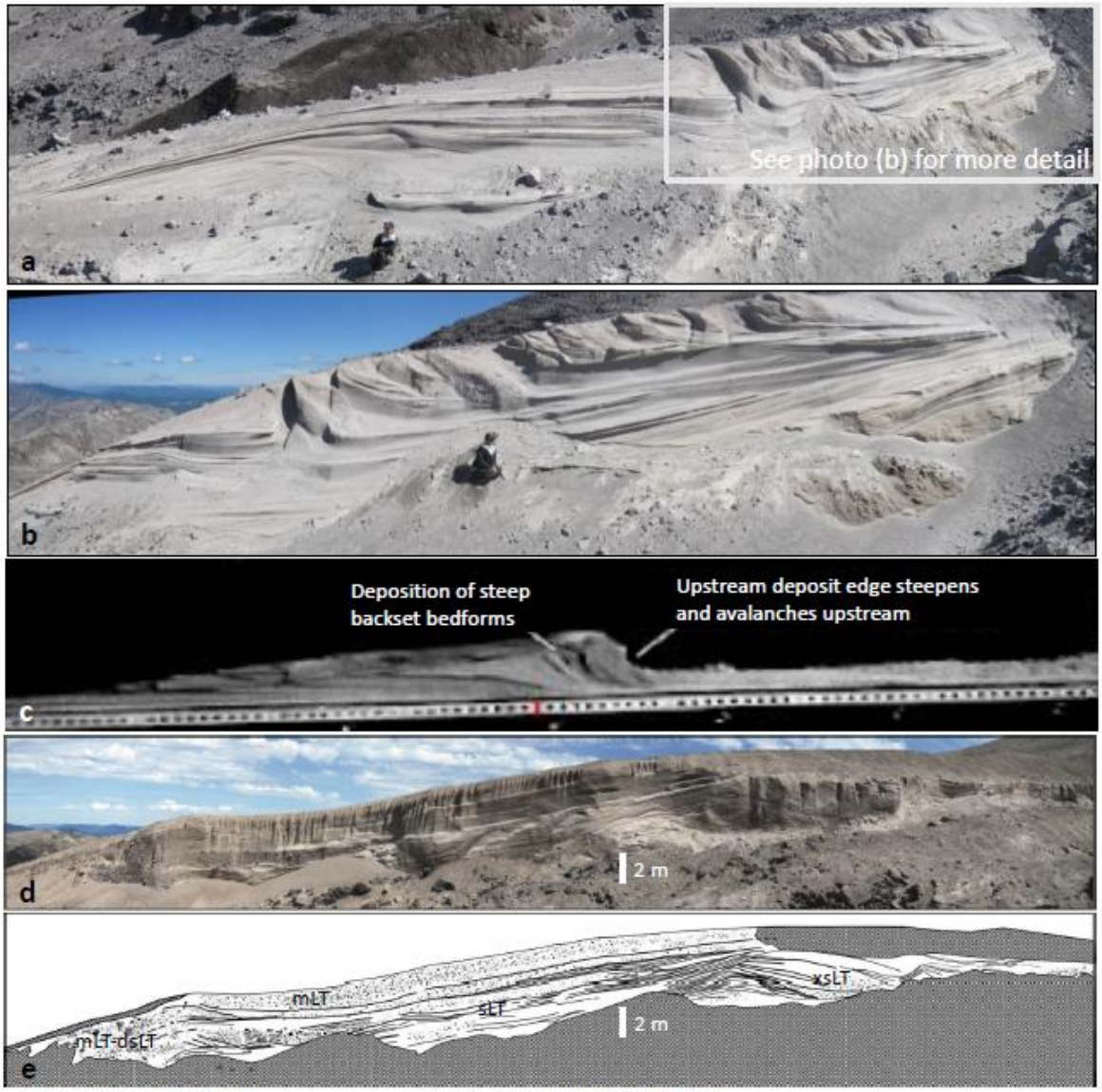

Figure 9: Flank deposits to eastern Pumice Plain. Flow direction is right to left for all panels, including the experiment snapshot in (c). Photos (a) and (b) show regressive bedforms with a series of steeply-dipping backset beds. (c) Photo from the experiments of Smith et al (2020) showing the development of a 'granular bore' and similar deposit features to (b). (d) and (e) Photograph and sketch of the transitional deposits found midflank. Photos in a and b are noted as PBD_1 for proximal deposit; photo in d is noted as PBD_2 for the transitional deposits (see locations in Figure 6).

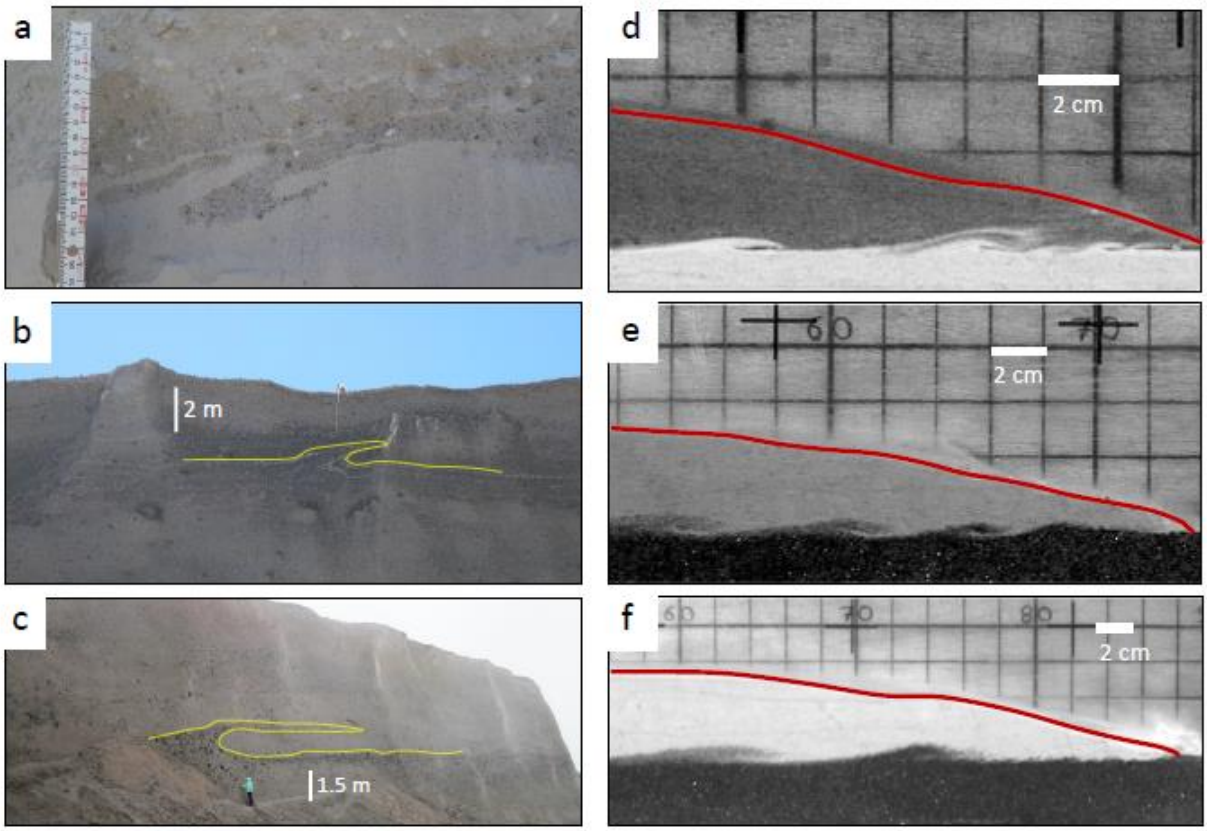

Figure 10: Examples of recumbent flame structures both within the 18 May 1980 PC deposits (a-c) and experimentally-produced structures (d-f; from Pollock 2019). Flow direction is left to right in all photographs. Yellow lines added to emphasize structures in (b) and (c). The locations of the structures found at MSH, named B-3 (a), C-4 (b), and AD-3 (c), respectively, are noted on the map in Figure 6. Note the increase in length of the experimentally-produced structures from 0.5-1.5 cm in panel 10d to 8-10 cm in panel 10f corresponding to increases in flow front velocity. Red line indicates flow top.

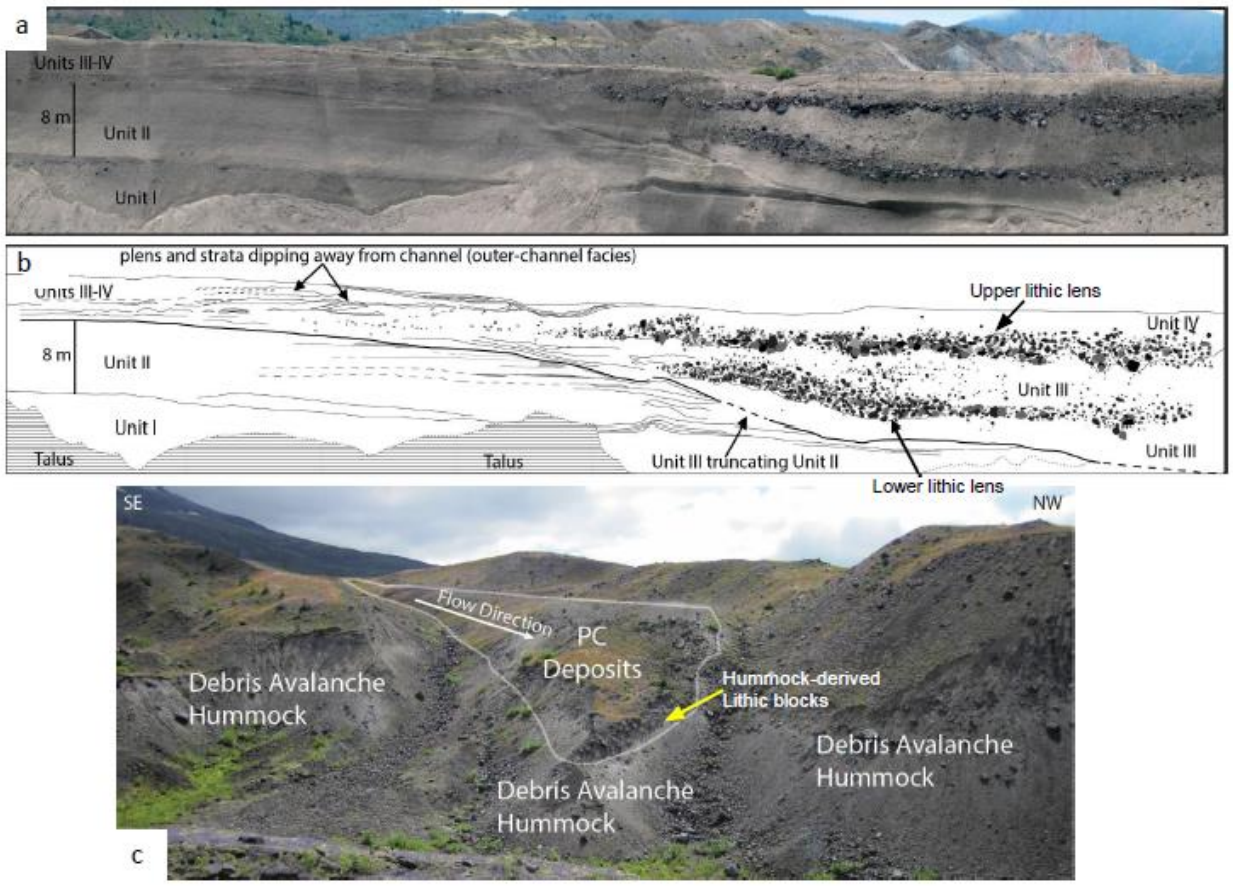

Figure 11: (a) and (b) show large scour and fill feature in the northwest Pumice Plain, associated with Units III and IV (modified from Brand et al., 2014). The lower block lens within the scour (Unit III) contains vent-derived lithics. The upper lithic lens was inaccessible for sampling. On left side of outcrop, pumice lens (plens) and strata dip away from the channel axis suggesting an outer-channel facies. Photo (c) shows a lithic-rich wedge of PC deposits nestled within a paleo-valley within the debris avalanche deposit (Location B-2 in Figure 6). The transparent white line denotes the contact between the debris avalanche hummock and the wedge of PDC deposits. The layer of lithics just above the debris avalanche contact was determined to be eroded from hummocks upslope (Brand et al., 2017).

Figure 12. Photograph looking eastward of Mount St. Helens erupting on July 22, 1980 at 19:01 PDT. The photo is taken at the beginning of the third eruptive pulse. A pyroclastic current moving rapidly northward from the crater is visible. U.S. Geological Survey photograph taken by J. Vallance.

Figure 13. Photograph showing pyroclastic-flow deposit of July 22, 1980 at Mount St. Helens. The photograph illustrates early stage spreading, multiple nested levee pairs, and complex sequence of late-stage, overlapping lobes. U.S. Geological Survey photograph taken by N. Macleod.

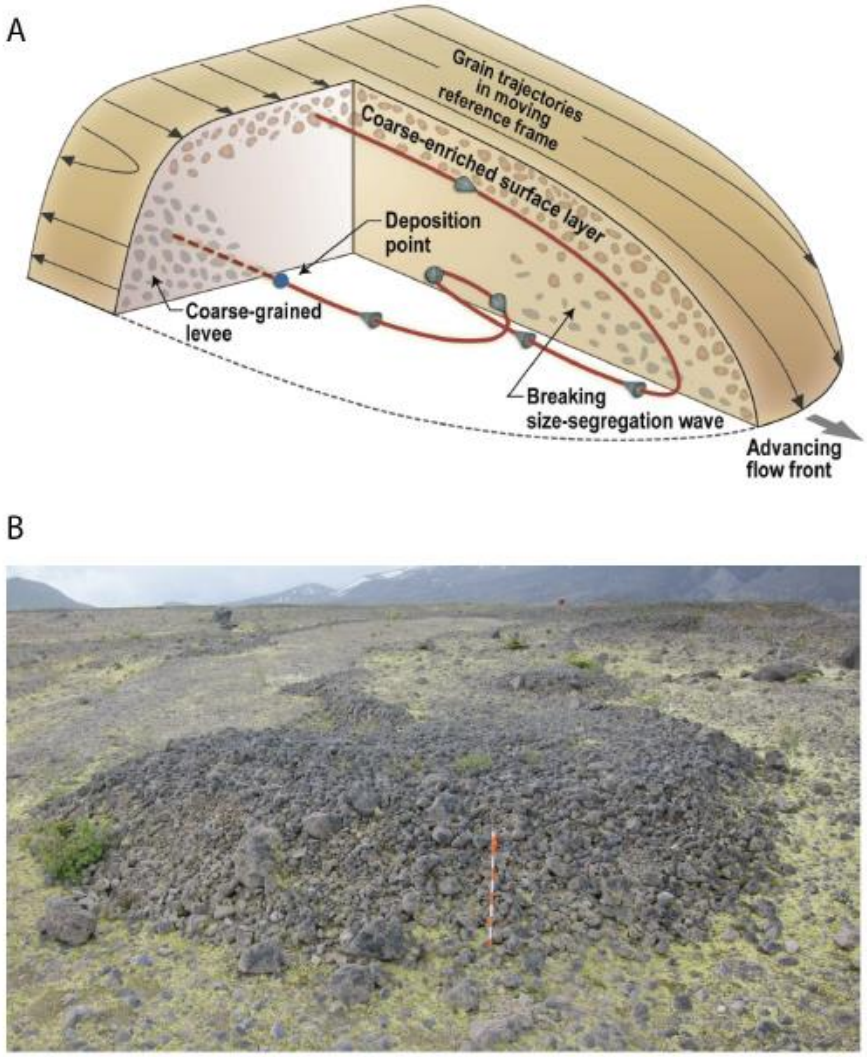

Figure 14. A. Schematic cutaway illustration of the process leading to formation of lateral levées behind a debris flow front. Red path shows how coarse grain near surface migrates toward a levée. Reference frame moves at speed of advancing flow so that a grain advancing less rapidly than flow front appears to move backwards (see Johnson et al., 2012). Coarse particles in a granular pyroclastic flow circulate in a fashion similar to that in a debris flow to form lobate termini and levees. B. Lobe of July 1980 pumiceous PC deposit on the Pumice Plain at Mount St. Helens (photographed in 2010). The flow-head deposit shows characteristic bulbous form, about 1 m thick (pole is 1 m), while the levées behind maintain the same form and grain-size characteristics as they bound channel-flow deposit for >250 m into the distance. Sparse meter-scale boulders between the levées (middle distance) are a stranded 'bed-load' of relatively dense rock presumed to have rolled or slid along the channel driven and partially supported by the channel-flow mixture. The substrate slope is approximately 4°. Adapted from Pallister et al. (2017).

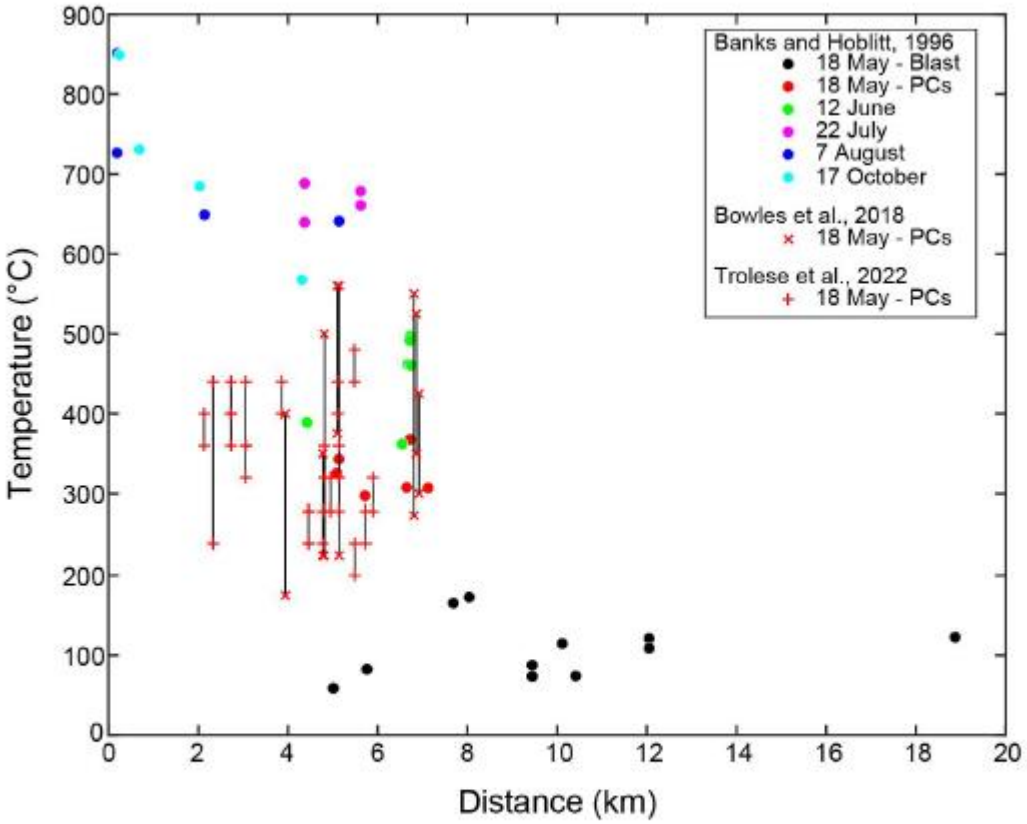

Figure 15: Collection of emplacement temperature data from the 1980 MSH eruptions.

Supplementary Figure 1: Isopach map of Unit 1. Lines outlined in black delimit topographic highs where no PC deposits exist (i.e. thickness of deposits inside these emboldened lines is zero).

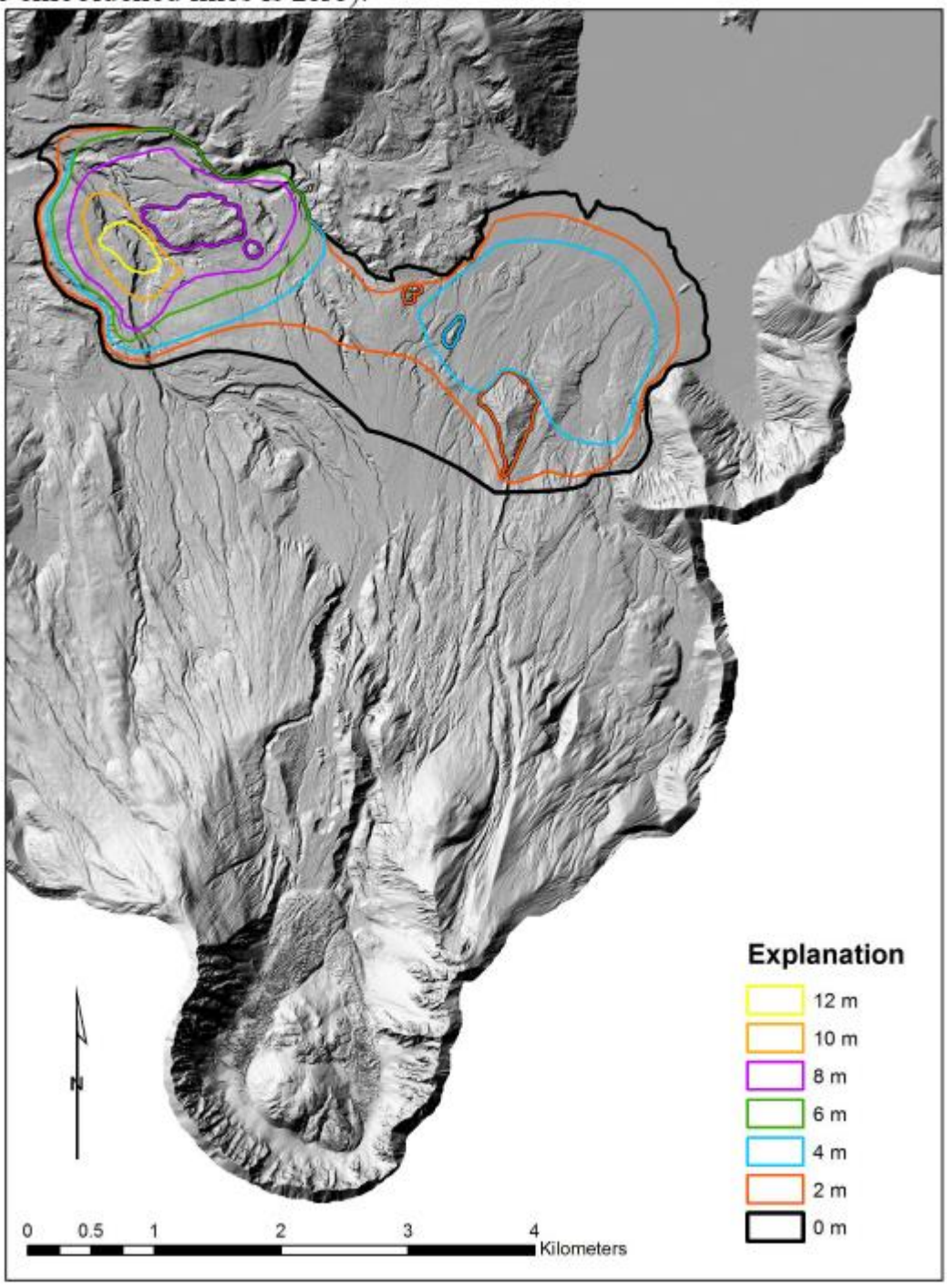

Supplementary Figure 2: Isopach map of Unit 2. Lines outlined in black delimit topographic highs where no PC deposits exist (i.e. thickness of deposits inside these emboldened lines is zero).

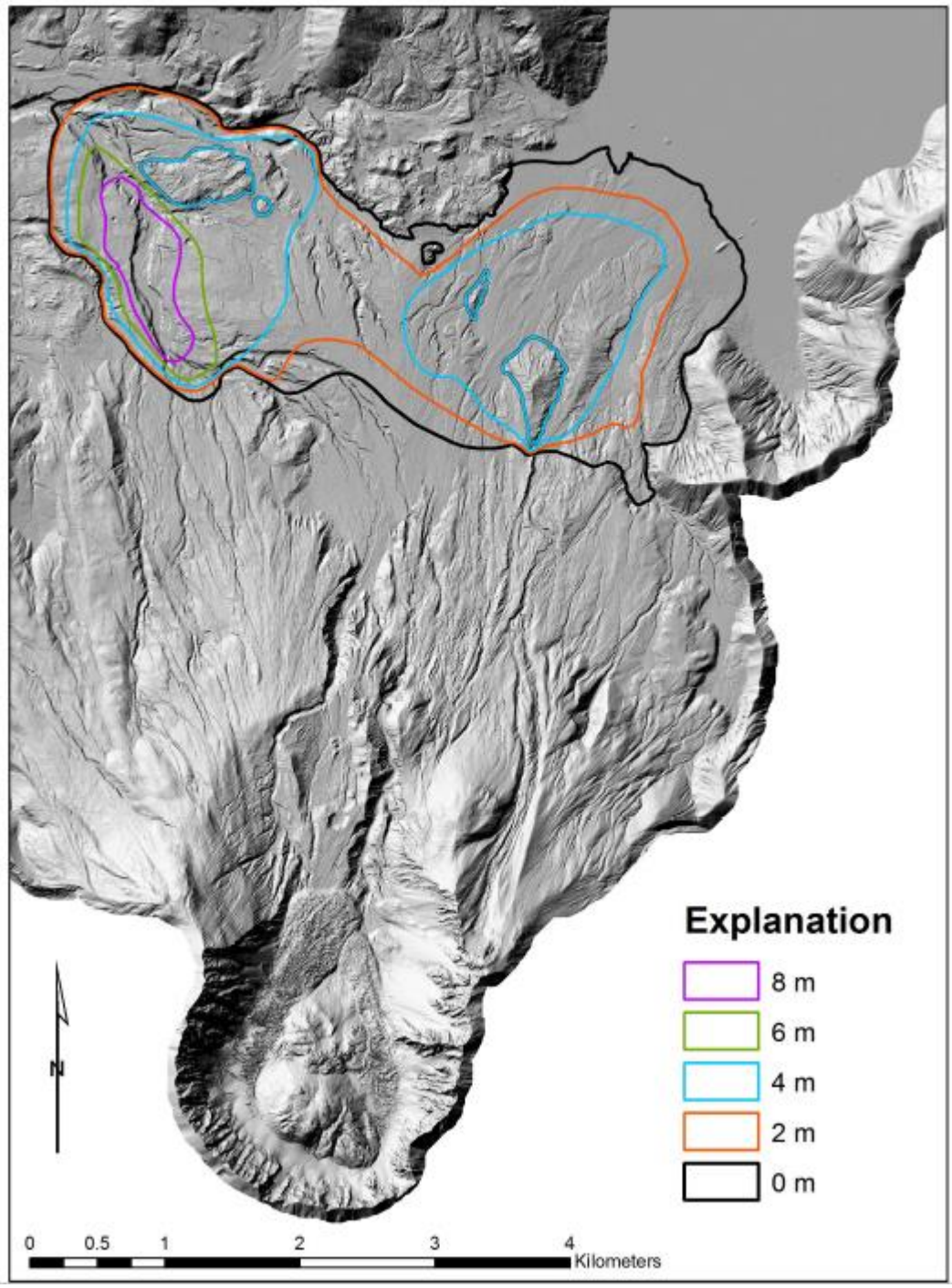

Supplementary Figure 3: Isopach map of Unit 3. Lines outlined in black delimit topographic highs where no PC deposits exist (i.e. thickness of deposits inside these emboldened lines is zero).

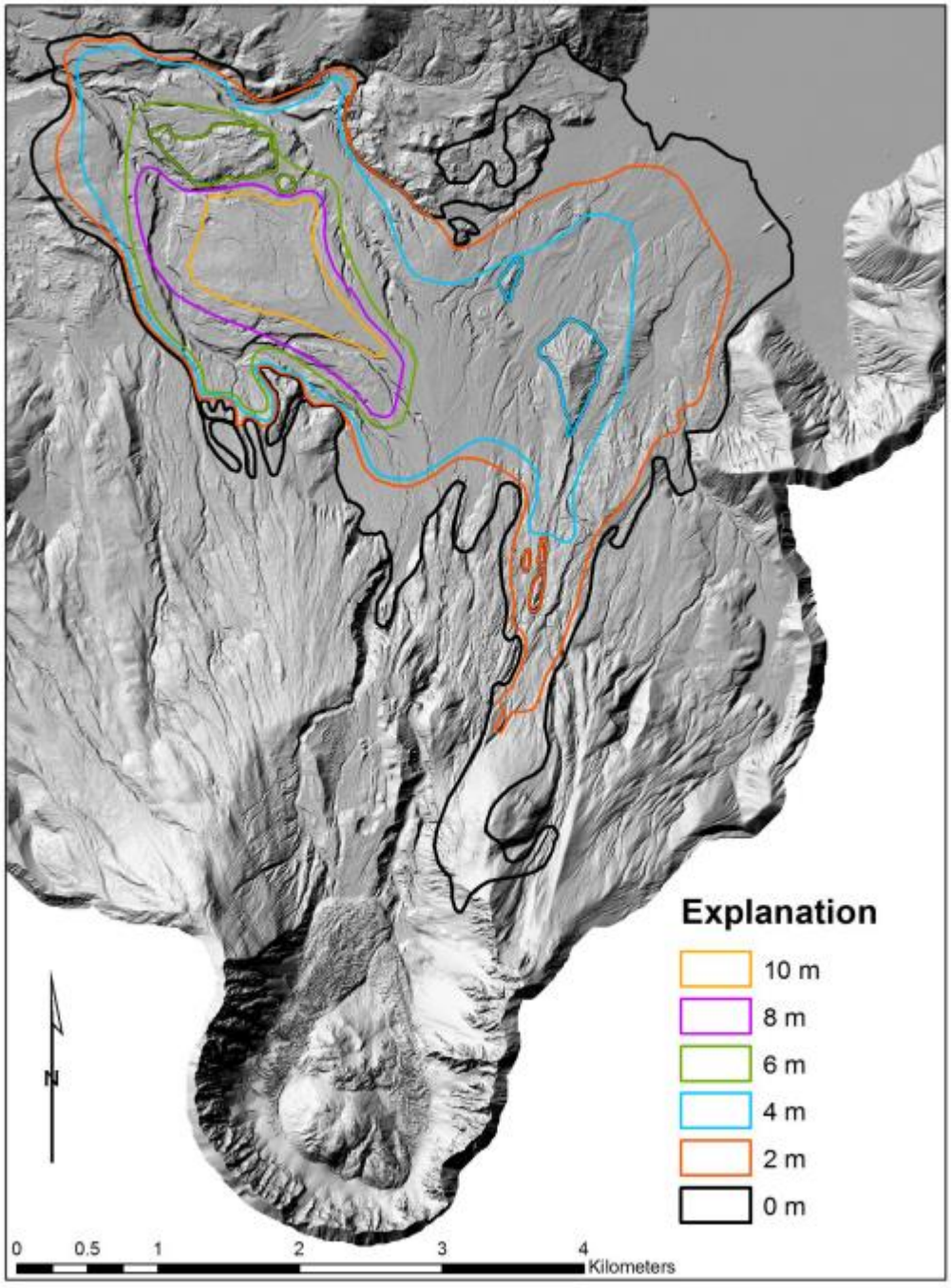

Supplementary Figure 4: Isopach map of Unit 4. Lines outlined in black delimit topographic highs where no PC deposits exist (i.e. thickness of deposits inside these emboldened lines is zero).

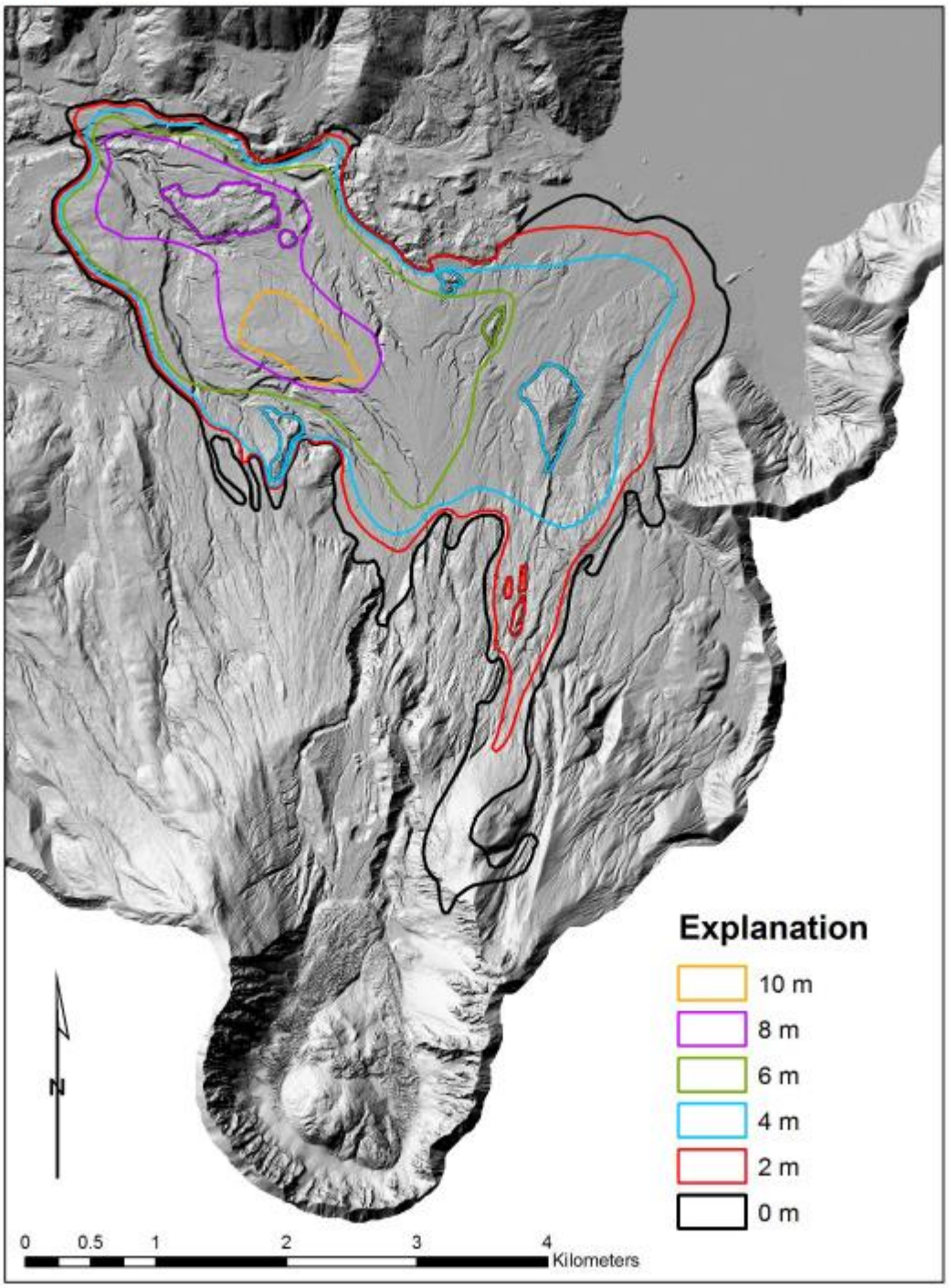

Supplementary Figure 5: PC volume for each unit is the integration of the area under each curve.